Coupled Adjoint-based Sensitivity Analysis using a FSI Method in Time Spectral Form

Hyunsoon Kim

Dissertation submitted to the Faculty of the

Virginia Polytechnic Institute and State University

in partial fulfillment of the requirements for the degree of

Doctor of Philosophy

in

Aerospace Engineering

Seongim S Choi, Chair

Pradeep Raj

Kevin G Wang

Dong S Ha

Aug 16, 2019

Blacksburg, Virginia

Keywords: Fluid Structure Interface(FSI), Design Optimization, Sensitivity, Adjoint method, Time Spectral Method

Coupled Adjoint-based Sensitivity Analysis using a FSI Method in Time Spectral Form

Hyunsoon Kim

(ABSTRACT)

A time spectral and coupled adjoint based sensitivity analysis of rotor blade is carried out in this study. The time spectral method is an efficient technique to solve unsteady periodic problems by transforming unsteady equation of motion to a steady state one. Due to the availability of the governing equations in the steady form, the steady form of the adjoint equations can be applied for the sensitivity analysis of the coupled fluid-structure system. An expensive computational time and memory requirement for the unsteady adjoint sensitivity analysis is thus avoided. A coupled analysis of fluid, structural, and flight dynamics is carried out through a CFD/CSD/CA coupling procedure that combines FSI analysis with enforced trim condition. Coupled sensitivity analysis results and their validations are presented and compared with aerodynamics only sensitivity analysis results. The fluid-structure coupled adjoint based sensitivity analysis will be applied to the shape optimization of a rotor blade in the future work. Minimization of required power is the objective of the optimization problem with constraints on thrust and drag of the rotor. The bump functions are considered as the design variables. Rotor blade shape changes are obtained by using the bump function on the surface of the airfoil sections along the span.

Coupled Adjoint-based Sensitivity Analysis using a FSI Method in Time Spectral Form

Hyunsoon Kim

(GENERAL AUDIENCE ABSTRACT)

The work in this dissertation is motivated by the reducing the computational cost at the early design stage with guaranteed accuracy. In the research, the author proposes that the goal can be achieve through coupled adjoint based sensitivity analysis using a fluid structure interaction in time spectral form. Adjoint based sensitivity analysis is very efficient for solving design problems with a large number of design variables. The time spectral approach is used to overcome inefficient calculation of rotor flows by expressing flow and structural state variables as Fourier series with small number of harmonics.

The accuracy and the efficiency of flow solver are examined by simulating UH-60A forward flight condition. A significant reduction in the computational cost is achieved by its Fourier series form of the periodic time response and the assumption of periodic steady state. A good agreement between time accurate and time spectral analysis is noted for the high speed forward flight condition of UH-60A configuration. Prediction from both methods also agree quite well with the experimental data. The adjoint based sensitivity analysis results are compared with the finite difference sensitivity analysis results. Even with presence of small discrepancies, these two results show a good agreement to each other. Coupled sensitivity analysis includes not only the effect of fluid state changes but also the contribution of structural deformation.

Contents

List of Figures

List of Tables

List of Abbreviations

Symbols

α_s	forward shaft tilt angle
$\bar{\mathbf{C}}$	modal damping matrix
$\bar{\mathbf{F}}$	modal load vector
$\bar{\mathbf{K}}$	modal stiffness matrix
$\bar{\mathbf{M}}$	modal mass matrix
$\mathbf{\Phi}$	mode shape matrix, eigenvector
$\phi_{\mathbf{a}}$	adjoint parameter for structure
$\psi_{\mathbf{a}}$	adjoint parameter for aero
$\mathbf{C}$	damping matrix
$\mathbf{F}$	force vector
$\mathbf{K}$	stiffness matrix
$\mathbf{M}$	mass matrix
$\mathbf{q}$	displacement vector
$\mathbf{R}$	time spectral form of fluid residuals
$\mathbf{S}$	time spectral form of structural residuals

$\mathbf{T}$	kinetic energy
$\mathbf{U}$	strain energy
$\mathbf{w(t)}$	time spectral form of fluid state
$\mathbf{y(t)}$	time spectral form of structural state
$\delta\mathbf{T}$	variation of kinetic energy
$\delta\mathbf{U}$	variation of strain energy
$\delta\mathbf{W}$	virtual work done by external forces
λ_T	warp function
$_0$	averaged mass per unit length (reference mass)
μ	advance ratio
Ω	rotational speed
ω_0	fundamental frequency
ϕ_i	elastic twist at ith structural node
ϕ_s	lateral shaft tilt angle
ψ	azimuth angle
σ	solidity
τ	pseudo time
θ	trim control input
θ_{1c}	lateral cyclic pitch angle

θ_{1s}	longitudinal cyclic pitch angle
θ_{75}	collective pitch angle at 75 percent radius
θ_{tr}	tail rotor collective pitch angle
b	design variable
C_w	vehicle weight coefficient
D	Fourier spectral derivative operator
e_A	distance of tensile center ahead of elastic axis
e_d	distance of aerodynamic center aft of elastic axis
e_G	distance of center of gravity ahead of elastic axis
EA	axial stiffness
EI_y	bending stiffness with respect to y axis
EI_z	bending stiffness with respect to z axis
f_a	aerodynamic force
GJ	torsional stiffness
I	objective function
k_A^2	Radius of gyration square (elastic)
k_{m1}^2	Radius of gyration square (mass)
k_{m2}^2	Radius of gyration square (mass)
N_H	the number of harmonics

p	pressure
R	fluid residuals
S	structural residuals
s_x	mesh metrics
t	time
u_i	axial deflection at ith structural node
v_i	lag bending deflection at ith structural node
$w(t)$	fluid state
w_i	flap bending deflection at ith structural node
x	mesh state
x_s	surface mesh
x_v	volume mesh
$y(t)$	structural state

Abbreviations

ALE	Arbitrary Lagrangian Eulerian
CA	Comprehensive Analysis
CAMRAD	Comprehensive Analytical Model of Rotorcraft Aerodynamics and Dynamics
CFD	Computational Fluid Dynamics
CSD	Computational Structural Dynamics

FDM	Finite Difference Method
FEM	Finite Element Method
FPR	Full Potential Rotor code
FSI	Fluid Structure Interaction
nTS	number of time instances in Time Spectral method
RANS	Reynolds-Averaged Navier-Stokes equations
RCAS	Rotorcraft Comprehensive Analysis System
SUmb	Stanford University multi-block
TA	Time Accurate analysis
TS	Time Spectral analysis
TSD	Transonic Small Disturbance
UMARC	University of Maryland Advanced Rotorcraft Code

Chapter 1

Introduction

Carrying out shape optimization of rotor blades is a difficult work due to the complex and unsteady nature of the air flow around the rotor blades. While accurately predicting the flow physics is essential for accurate design, it can be computationally expensive. Additionally, the fluid dynamic analysis also needs to be coupled with structural and flight dynamic analysis to accurately capture the rotor deformation and subsequently carry out reliable design. This makes the rotor design process complicated and time consuming. Therefore, existing rotorcraft comprehensive analysis tools generally use low-fidelity aerodynamic models to generate air-load on the rotor blade, such as the lifting line theory and the vortex wake model. The objective of this study is to develop an accurate and efficient sensitivity analysis method for helicopter rotor blades by using high fidelity unsteady Euler equations to model the fluid analysis and to couple it with structural and flight dynamic analysis. To efficiently compute the unsteady nature of the fluid and structural governing equations, the time spectral method has been used and coupled adjoint-based sensitivity analysis has been developed and applied to carry out sensitivity analysis of rotor blades in forward flight condition.

1.1 CFD/CSD coupling

For FSI analysis, the CFD and CSD solvers can be coupled by either loose coupling or tight coupling. The differences in these coupling strategies are briefly summarized in how data are exchanged and tracked by the CFD and CSD modules. In loose coupling, separately fully converged airloads and structural displacements are exchanged, while in tight coupling, all the aerodynamic and structural dynamic equations are converged simultaneously through pseudo time iteration. In loose coupling, the converged pressure distribution on the rotor blade is transferred for the entire revolution from the CFD to CSD module and the structural deformation is transferred back from the CSD to CFD module, again, for the entire revolution. The main advantage of this method is that it converges in a few (7$\sim$8) FSI iterations. Due to its simplicity, the method was the first approach to be widely used for solving rotor aeroelastic problems. The tight coupling is a direct approach to solve coupled CFD and CSD equations. Tightly coupled two codes must run concurrently. Although tight coupling is computationally expensive, it is a more rigorous strategy which integrates fluid/structural equations simultaneously at each step.

1.2 Time Spectral Method

The time spectral approach is an efficient method based on the Fourier collocation method. It approximates the periodic solution by a Fourier series expansion and applies the collocation method to replace the time derivative term in the governing equations by a simple matrix-vector product form known as the time spectral derivative operator. The time spectral method does not require transient calculation to reach the periodic steady state. The benefit of using time spectral method compared to frequency domain methods is that it solves the governing equations directly in the time-domain and removes the process of transforming the flow solutions between the frequency and time domain. Time spectral method is well suited to analyze unsteady periodic problems, such as helicopter rotor flow analysis.

1.3 Adjoint-based Sensitivity Analysis

The use of adjoint method has become a popular approach for solving design optimization problems. The adjoint based sensitivity analysis is cost effective as it can inexpensively compute the sensitivity of an object with respect to a large number of design inputs. The cost of sensitivity calculation is similar to the cost of a single analysis, which is unlike the finite difference method, where the computational cost is proportional to the number of design variables times the analysis cost. However, the application of the adjoint method to the unsteady problem has been limited when the objective is a time averaged function and the formulation of the adjoint method is dependent on the time integration method. The flow and structural residuals, Jacobians, and adjoint variables should be stored at each time step, requiring prohibitive amount of memory. This problem is further complicated when carrying out sensitivity analysis for multidisciplinary coupled systems such as FSI problems. There are two approaches to formulate the adjoint for a set of partial differential equations. They are the continuous adjoint approach and the discrete adjoint approach. The continuous adjoint approach consists of differentiating the partial differential equations analytically to get the PDE form of the adjoint equations, which are then discretized so that they can be solved numerically. However, the discrete adjoint approach starts with the discretized form of the partial differential equations, which is then linearized to obtain the discrete adjoint equations, which are a set of linear equations. The advantage of the continuous adjoint approach is that it generates a linearized partial differential equation that can be solved by using the same numerical iteration technique as the flow solution. This eliminates the need to explicitly form the Jacobian and leads to fast and low memory adjoint implementations [1, 2]. However, the disadvantages of the continuous adjoint approach are a low accuracy for coarser meshes and a challenging implementation. The fact that the PDEs are first linearized and then discretized means that the discretized form of these equations is guaranteed to result in a fully consistent gradient only at the limit of an infinitely fine mesh [3]. Therefore, the continuous adjoint produces inaccurate gradient for cases where the mesh or the numerical methods have an effect on the solution accuracy [4]. For these reasons, the discrete adjoint approach is used in this study.

1.4 Thesis Objectives

The aim of the current work is to extend the previous work of Choi, et. al. [5], where rotor shape design was performed with the prescribed rotor blade deformations and trim angles. While the previous work offered simplicity and speedy computations, it involves only the aerodynamic analysis and requires measured or pre-computed deformation and trim control inputs. In this study, a coupled analysis of fluid, structural, and flight dynamics is carried out through a CFD/CSD/CA coupling procedure that combines the FSI analysis with enforced vehicle trim condition. Following which, the coupled adjoint based sensitivity analysis is performed for the fluid-structure system. The adjoint based sensitivity analysis is validated by comparing with the finite difference method based sensitivity analysis results. Also, the fluid-structure coupled sensitivity analysis results for the fluid-structure system are compared with the aerodynamics only sensitivity analysis results to show the contribution of structural deformation to the sensitivity analysis.

Chapter 2

Review of Literature

2.1 CFD/CA coupled FSI Analysis

Current comprehensive analysis tools for rotorcraft use simplified aerodynamic models such as lifting line theory, which are based on the the relative movement of the each section with respect to the flows [6]. The sectional angle of attack changes are computed based on the rotor blade twist, the free-stream velocities, and the wake induced velocities. The aerodynamic model calculates the pressure distribution on the surface of the airfoil which generates airloads. However, high fidelity CFD can be used to calculate more accurate and detailed pressure distributions. Though CFD has higher computational cost, increasing computational power and parallelization have enabled the use of CFD in such practical applications. Coming to the structural dynamic model, the linear coupled (axial deflection, lead-lag bending, flap bending and torsion) structural dynamics of rotor were shown by Houbolt et al. [7]. Ormiston and Hodges [8] used a spring hinge to include the effect of centrifugal nonlinearities. A set of coupled, nonlinear structural equations of motion for large deformations was derived by Hodges and Dowell [9]. Hodges et al. [10] developed nonlinear expressions to relate the orientation of the deformed-beam cross section, torsion, local components of bending curvature, angular velocity, and virtual rotation to deformation variables. This development helps to clarify the nature of the elastic torsion variable which is treated as a quasi-coordinate. These formulations are extended to include the nonlinear structural and inertial effects for large deformation by Kvaternik et al. [11], Rosen and Freidmann [12]. The structural governing equations are discretized by using finite element method [13, 14]. The rotor blade structural FEM model that includes the nonlinear terms are used in this study. A comprehensive analysis(CA) should have the essential component models (including the structural FEM model) to solve the multidisciplinary nature of helicopter problems. The CA code need to compute airloads, structural deformation, trim control angles and stability. Examples of the CA code are CAMRAD [15], UMARC [6] and RCAS [16]. As mentioned in the introduction, coupling between CFD/CSD can be accomplished in two ways. In loose coupling, airloads and structural deformation are interchanged between aerodynamic and structural model once every revolution. Tung et al. [17] developed the first CFD/CSD loose coupling procedure. In this procedure, the comprehensive analysis provides the airloads sensitivities with respect to the rotor blade deformations that act as aerodynamic damping, providing faster convergence. This procedure is called as the delta method. Strawn and Desopper [18] combined a full potential equations based CFD solver with the CAMRAD/JA helicopter performance code. The influence of flow field unsteadiness is found to play an important role in the blade aerodynamics. Kim et al. [19] coupled a Transonic Small Disturbance based CFD model with UMARC. In this study, the coupled system proceeded updates of the vehicle trim and structural deformation during the coupling process and used both lift and pitching moment. Sitaraman et al. [20] coupled TURNS-3D and UMARC, and obtained flow solution with a prescribed deformation of the UH-60A at high speed forward flight condition. Potsdam et al. [21] coupled OVERFLOW-D with CAMRAD-II. Their CFD code used a high fidelity overset grid methodology with wake capturing. They calculated the UH-60A Blackhawk helicopter rotor airloads across a range of flight conditions. In the time accurate tight coupling approach, the CFD and CSD codes are coupled at every time step and integrated simultaneously. Although tight coupling is more rigorous, care should be taken to ensure timewise accuracy between CFD and CSD. Also, code modification may be required for efficient communications between CFD and CSD. Altmikus et al. [22] made a comparison of two coupling strategies. They showed that tight coupling is 2.5 times computationally expensive than loose coupling. Bauchau et al. [23] made tightly coupled calculation and observed large differences between the prediction of the rigid blade and aeroelastic cases. This demonstrates the need for coupling CFD and CSD for rotorcraft comprehensive analysis. Pomin et al. [24] presented a numerical approach for the aeroelastic analysis of helicopter rotor based on the RANS equations and Timoshenko beam theory. The tightly coupled procedure was applied to generate hover performance data for the ONERA 7A model rotor on periodic structured grids.

2.2 Adjoint-based Sensitivity Analysis

The use of adjoint method has become a popular approach for solving aerodynamic shape-optimization problems using computational fluid dynamics [25, 26, 27]. This is largely due to the fact that the adjoint based sensitivity analysis is cost effective as it can inexpensively compute the sensitivity of an objective with respect to a large number of design inputs. The cost of sensitivity calculation is similar to that of the analysis, which is unlike the finite difference method, where the computational cost is proportional to the number of design variables times the analysis cost. The computational cost of adjoint method is independent of the number of design variables. However, the application of the adjoint method to unsteady problem has been limited when the objective is a time dependent function and the formulation of the adjoint method is dependent on the time integration method. The flow residuals, Jacobians, and adjoint variables have to be stored at each time step, requiring prohibitive amount of memory. Mavriplis [28] demonstrated the formulation and solution of the adjoint problem for unsteady flow simulations using the Reynolds-averaged Navier-Stokes equations. Full implementation and application to large-scale problems including helicopter rotor problem were made by Lee and Kwon [29], and by Nielsen et al. using NASA FUND3D code [30, 31]. This problem is further complicated when carrying out sensitivity analysis for FSI problems. The coupled adjoint based sensitivity analysis and design optimization for static aeroelasitc problems has been shown by Martins et al. [32, 33, 34]. Maute et al. [35, 36] calculated the sensitivity of a steady coupled aerodynamic structural system by both direct and adjoint method. Mishra et al. [37, 38] have computed the sensitivity of coupled time dependent aeroelastic systems for the purpose of shape optimization of helicopter rotors in hover and forward flight conditions.

2.3 Time Spectral Method

Time spectral method has been used as an efficient approach for the simulation of periodic problems. Gopinath, Weide and Jameson [39, 40, 41] proposed the time spectral algorithm for the fast and efficient computation of time periodic turbulent Navier-Stokes calculations past two and three dimensional bodies. Time spectral method has been applied to a large number of applications such as turbo-machinery and flapping wings. Hall et al. [42] and Jameson et al. [43] introduced time spectral concept to aerodynamic analysis which was successfully applied to rotor flight [44], open rotor [45] problems. Helicopter rotor flow is an appropriate application of the time spectral method due to the periodic nature of rotor flows. Choi et al. [46, 47, 48, 49] applied time spectral approach to rotor flow analysis. All these works have validated the applications of the time spectral method on a UH-60A Black Hawk helicopter rotor for several flight conditions. Prasad et al. [50] have developed a discrete adjoint approach for aeroelastic design sensitivities based on the time spectral method. He et al. [51] applied Euler time-spectral computational fluid dynamics methods to model the flutter constraint and proposed a coupled adjoint method to calculate the constraint sensitivity with respect to the design variables.

Chapter 3

Aerodynamic Model for Rotor Flows

3.1 Governing Equations

The Euler equations have been applied to inviscid compressible flow. The Arbitrary Lagrangian Eulerian (ALE) form of the Euler equations has been considered to accommodate moving boundaries and mesh motion. Eq. (3.1)- Eq. (3.5) shows the 3-dimensional Euler equations in conservation form.

$$\frac{\partial \rho}{\partial t} + \frac{\partial(\rho(u-u_x))}{\partial x} + \frac{\partial(\rho(v-v_x))}{\partial y} + \frac{\partial(\rho(w-w_x))}{\partial z} = 0 \tag{3.1}$$

$$\frac{\partial \rho u}{\partial t} + \frac{\partial(\rho u(u-u_x)+p)}{\partial x} + \frac{\partial(\rho u(v-v_x))}{\partial y} + \frac{\partial(\rho u(w-w_x))}{\partial z} = 0 \tag{3.2}$$

$$\frac{\partial \rho v}{\partial t} + \frac{\partial(\rho v(u-u_x)}{\partial x} + \frac{\partial(\rho v(v-v_x)+p)}{\partial y} + \frac{\partial(\rho v w(w-w_x))}{\partial z} = 0 \tag{3.3}$$

$$\frac{\partial \rho w}{\partial t} + \frac{\partial(\rho w(u-u_x))}{\partial x} + \frac{\partial(\rho w(v-v_x))}{\partial y} + \frac{\partial(\rho w(w-w_x)+p)}{\partial z} = 0 \tag{3.4}$$

$$\frac{\partial \rho e_t}{\partial t} + \frac{\partial(\rho e_t(u-u_x)+pu)}{\partial x} + \frac{\partial(\rho e_t(v-v_x)+pv)}{\partial y} + \frac{\partial(\rho e_t(w-w_x)+pw)}{\partial z} = 0 \tag{3.5}$$

where u,v and w are the fluid velocities in x,y and z directions respectively, and u_x, v_x and w_x are the grid velocities. These equations can be expressed in a simple vector form as follows

$$V\frac{\partial \mathbf{w}}{\partial t} + \mathbf{R}(\mathbf{w}) = 0 \tag{3.6}$$

where $\mathbf{w}$ is the fluid state vector, and $\mathbf{R}(\mathbf{w})$ is the residual vector of Euler Equations.

$$\mathbf{w} = \begin{Bmatrix} \rho \\ \rho u \\ \rho v \\ \rho w \\ \rho e_t \end{Bmatrix} \tag{3.7}$$

3.2 Unsteady Flows in Time Spectral Form

The time-spectral approach has been used to overcome inefficient calculations by assuming the periodic behavior of fluid. The fluid state variables are expressed as Fourier series with a small number of harmonics. The advantage of the time spectral method is that it converts unsteady problem to steady problem by removing time derivative terms. Then it can reduce computing cost with accurate prediction capabilities. The basic concept of the time spectral method is expressing the fluid state variables $w(t)$ in terms of a discrete Fourier series as shown in Eq. (3.8). The unsteady inviscid compressible Euler equations in time domain shown in Eq. (3.6) are converted to the frequency domain using N_H number of harmonics and transformed into the time domain using $2N_H + 1$ number of time instances (collocation points). Then the time spectral form of the aerodynamic governing equations can be written as Eq. (3.9). The fundamental frequency ω_0 is the rotor rotating speed and used to expand the Fourier series expansion.

$$w(t) = \hat{w}_0 + \sum_{n=1}^{N_H} (\hat{w}_{cn} cos(\omega_0 nt) + \hat{w}_{sn} sin(\omega_0 nt)) \tag{3.8}$$

$$\omega_0 V \mathbf{D} \mathbf{w_{ts}} + \mathbf{R_{ts}} = 0 \tag{3.9}$$

where, $\mathbf{w_{ts}}$ and $\mathbf{R_{ts}}$ represent a set of flow variables and their residuals at collocation points, respectively.

$$\mathbf{w_{ts}} = \begin{Bmatrix} w(t_0 + \Delta t) \\ w(t_0 + 2\Delta t) \\ ... \\ w(t_0 + T) \end{Bmatrix}, \mathbf{R_{ts}} = \begin{Bmatrix} R(t_0 + \Delta t) \\ R(t_0 + 2\Delta t) \\ ... \\ R(t_0 + T) \end{Bmatrix} \tag{3.10}$$

Steady state form of Eq. (3.9) can be solved using pseudo-time iteration method. Eq. (3.9) can be written as Eq. (3.11) with the addition of the pseudo time derivative term for convergence.

$$\frac{d\mathbf{w_{ts}}}{d\tau} + \omega_0 V \mathbf{D} \mathbf{w_{ts}} + \mathbf{R_{ts}} = 0 \tag{3.11}$$

The method is implemented in the flow solver of SUmb (Stanford University multi-block). Spatial numerical flux is discretized using the JST scheme [52], and the time step is marched using multi-stage Runge-Kutta method to obtain a steady-state solution in pseudo time.

3.3 Spectral Derivative Matrix

The derivation of the time spectral matrix, $\omega_0 D$, is described in this section to show the difference between the aerodynamic and structural governing equations in time spectral form. More details of the time spectral method and its derivation can be found in the work of Naik [53]. The Fourier transform of a signal $p(t)$ gives information about its spectrum. That is, the time domain function is transformed into the frequency domain function. If $p(t)$ is a discrete periodic signal of length N

$$p[j] \quad j = 0, 1, 2, ..., N-1 \tag{3.12}$$

The k-th component of its discrete Fourier transform is

$$P_k = \frac{1}{N}\sum_{j=0}^{N-1} p[j]e^{-2\pi ikj/N} \tag{3.13}$$

The discrete $p[j]$ is defined over N time instances and spans a physical time period T. The time vector is uniformly spaced starting from zero time. As a result, this following relations hold

$$\frac{t_j}{T} = \frac{j}{N},\ T = t_N \tag{3.14}$$

Then the k-th component of discrete Fourier transform, P_k, becomes

$$P_k = \frac{1}{N}\sum_{j=0}^{N-1} p[j]e^{-2\pi ikt_j/T} \tag{3.15}$$

P_k is defined over the discrete frequencies, k. However, the time derivative needs to be taken in the time domain. The inverse discrete Fourier transform of P_k transforms the expression back to the time domain.

$$\begin{aligned} p[l] &= \sum_{k=0}^{N-1} P_k e^{2\pi i k t_l/T} \\ &= \sum_{k=-\frac{N-1}{2}}^{\frac{N-1}{2}} P_k e^{2\pi i k t_l/T} \end{aligned} \tag{3.16}$$

Taking the time derivative gives

$$\begin{aligned} \frac{\partial p[l]}{\partial t_l} &= \frac{\partial}{\partial t_l} \sum_{k=-\frac{N-1}{2}}^{\frac{N-1}{2}} P_k e^{2\pi i k t_l/T} \\ &= \frac{2\pi}{T} \sum_{k=-\frac{N-1}{2}}^{\frac{N-1}{2}} ikP_k e^{2\pi i k t_l/T} \\ &= \frac{2\pi}{T} \sum_{k=-\frac{N-1}{2}}^{\frac{N-1}{2}} ik\Big(\frac{1}{N}\sum_{j=0}^{N-1} p[j] e^{-2\pi i k t_j/T}\Big) e^{2\pi i k t_l/T} \\ &= \frac{2\pi}{T}\frac{1}{N} \sum_{k=-\frac{N-1}{2}}^{\frac{N-1}{2}} \sum_{j=0}^{N-1} ikp[j] e^{-2\pi i k t_j/T} e^{2\pi i k t_l/T} \\ &= \frac{2\pi}{T}\frac{1}{N} \sum_{k=-\frac{N-1}{2}}^{\frac{N-1}{2}} \sum_{j=0}^{N-1} ikp[j] e^{2\pi i k (t_l/T - t_j/T)} \\ &= \frac{2\pi}{T}\frac{1}{N} \sum_{k=-\frac{N-1}{2}}^{\frac{N-1}{2}} \sum_{j=0}^{N-1} ikp[j] e^{2\pi i k (l/N - j/N)} \\ &= \frac{2\pi}{T}\frac{1}{N} \sum_{k=-\frac{N-1}{2}}^{\frac{N-1}{2}} \sum_{j=0}^{N-1} ikp[j] e^{2\pi i k (l-j)/N} \\ &= \frac{2\pi}{T} \sum_{j=0}^{N-1} \left\{ \frac{1}{N} \sum_{k=-\frac{N-1}{2}}^{\frac{N-1}{2}} ik e^{2\pi i k (l-j)/N} \right\} p[j] \\ &= \omega_0 \sum_{j=0}^{N-1} D[l,j] p[j] \end{aligned} \tag{3.17}$$

where $\omega_0 = \frac{2\pi}{T}$, and $D[l, j]$ is the spectral matrix

$$D[l, j] = \frac{1}{N} \sum_{k=-\frac{N-1}{2}}^{\frac{N-1}{2}} ike^{2\pi ik(l-j)/N} \tag{3.18}$$

Eq. (3.17) shows that the time derivative of the discrete periodic signal, p, can be calculated by simply multiplied by $\omega_0 D$, where $\omega_0 = \frac{2\pi}{T}$, and D is the spectral matrix.

$$\frac{\partial p}{\partial t} = \omega_0 D p \tag{3.19}$$

Chapter 4

Structural Model of Rotor Blade

Chapter 4 describes the structural model of rotor blade. The rotor blade is modeled as a long, slender beam undergoing axial deflection, flap bending, lead-lag bending and torsional deformation. The structural model follows the Hodges and Dowell formulation [9]. The structural governing equations are derived by using Hamilton's principle. The full derivation of the governing equations is described in Datta's work [54]. The governing equations are spatially discretized by using Finite Element Method. The differential form of governing equation in time domain is converted to the frequency domain, and then the time spectral form of governing equation is derived at the end of this chapter.

4.1 Derivation of Governing Equations

A bend-twist beam model is a suitable and widely used structural model for slender rotor blades. A bend-twist beam model was developed and implemented in UMARC (University of Maryland Advanced Rotorcraft Code). Hamilton's principle says that the trajectory of a system, between two specified states at two specified times t_1 and t_2, is the stationary point of the time integration of the difference between the potential and kinetic energies. For an aeroelastic system, e.g. the helicopter rotor blade, there are non-conservative forces. The generalized Hamilton's principle, applicable to non-conservative systems, is expressed as

$$\delta\Pi = \int_{t_1}^{t_2} (\delta U - \delta T - \delta W)dt = 0 \tag{4.1}$$

Where δT is the variation of kinetic energy and δU is the variation of strain energy. δW is the virtual work done by external forces.

4.1.1 Coordinate Systems and Nondimensionalization

Two coordinate systems are used to describe the motion of rotor blade. The first one is the undeformed blade coordinate system, (x, y, z). The unit vectors of undeformed coordinate system are $\hat{i}, \hat{j}, \hat{k}$. The other is the deformed coordinate system, (ξ, η, ζ) with unit vector $\hat{i}_\xi, \hat{j}_\eta, \hat{k}_\zeta$. The coordinate transformation matrix between these two coordinate systems can be determined by the direction cosine between (ξ, η, ζ) and (x, y, z). The transformation matrix can be expressed as

$$\begin{Bmatrix} \hat{i}_\xi \\ \hat{j}_\eta \\ \hat{k}_\zeta \end{Bmatrix} = T_{DU} \begin{Bmatrix} \hat{i} \\ \hat{j} \\ \hat{k} \end{Bmatrix} \tag{4.2}$$

where T_{DU} is a function of three successive Euler angles.

All the structural analysis is done by solving nondimensional form of structural governing equation. Using nondimensional form of governing equation helps to avoid scaling problems and increase the generality of the analysis. The reference parameters that are used as the nondimensionalization factors are shown in Table 4.1.

The axial coordinate x is nondimensionalized by R, and the azimuth angle is considered as

Table 4.1: Nondimensionalization Reference Parameters

Length	R
Time	$1/\Omega$
Mass per Length	m_0
Velocity	ΩR
Acceleration	Ω^2 R
Force	$m_0\Omega^2 R^2$
Moment	$m_0\Omega^2 R^3$
Work	$m_0\Omega^2 R^3$

nondimensional time, therefore

$$\frac{\partial(\ )}{\partial x} = \frac{\partial(\ )}{\partial r}\frac{\partial r}{\partial x} = \frac{1}{R}\frac{\partial(\ )}{\partial r} \tag{4.3}$$

$$\frac{\partial^2(\ )}{\partial x^2} = \frac{1}{R^2}\frac{\partial^2(\ )}{\partial r^2} \tag{4.4}$$

$$\frac{\partial(\ )}{\partial t} = \frac{\partial(\ )}{\partial \psi}\frac{\partial \psi}{\partial t} = \Omega\frac{\partial(\ )}{\partial \psi} \tag{4.5}$$

$$\frac{\partial^2(\ )}{\partial t^2} = \Omega^2\frac{\partial^2(\ )}{\partial \psi^2} \tag{4.6}$$

4.1.2 Strain Energy

Due to the rotor blade being modeled as a long, slender beam element, the uni-axial assumption can be used.

$$\sigma_{yy} = 0 \tag{4.7}$$

$$\sigma_{zz} = 0 \tag{4.8}$$

$$\sigma_{yz} = 0 \tag{4.9}$$

The remaining constitutive relations are

$$\sigma_{xx} = E\epsilon_{xx} \tag{4.10}$$

$$\tau_{x\eta} = G\gamma_{x\eta} \tag{4.11}$$

$$\tau_{x\zeta} = G\gamma_{x\zeta} \tag{4.12}$$

where σ_{xx} and ϵ_{xx} are the axial stress and strain, and $\tau_{x\eta}$, $\tau_{x\zeta}$ and $\gamma_{x\eta}$, $\gamma_{x\zeta}$ means the transverse shear stress and strain. The strain energy of rotor blade can be expressed as

$$U = \int_0^R \iint_A (\sigma_{xx}\epsilon_{xx} + \tau_{x\eta}\gamma_{x\eta} + \tau_{x\zeta}\gamma_{x\zeta}) d\eta d\zeta dx \tag{4.13}$$

The variation of strain energy can be calculated by using stress-strain relation.

$$\delta U = \int_0^R \iint_A (E\epsilon_{xx}\delta\epsilon_{xx} + G\gamma_{x\eta}\delta\gamma_{x\eta} + G\gamma_{x\zeta}\delta\gamma_{x\zeta}) d\eta d\zeta dx \tag{4.14}$$

The nonlinear strain-displacement relations up to second order (Hodges and Dowell [9]) are

$$\begin{aligned} \epsilon_{xx} = u' + \frac{v'^2}{2} + \frac{w'^2}{2} - \lambda_T\phi'' + (\eta^2 + \zeta^2)(\theta'\phi' + \frac{\phi'^2}{2}) \\ -v''[\eta cos(\theta + \phi) - \zeta sin(\theta + \phi)] \\ -w''[\eta sin(\theta + \phi) + \zeta cos(\theta + \phi)] \end{aligned} \tag{4.15}$$

$$\gamma_{x\eta} = -\frac{1}{2}(\zeta + \frac{\partial \lambda_T}{\partial \eta})\phi' = -\hat{\zeta}\phi' \tag{4.16}$$

$$\gamma_{x\zeta} = \frac{1}{2}(\eta - \frac{\partial \lambda_T}{\partial \zeta})\phi' = \hat{\eta}\phi' \tag{4.17}$$

where λ_T is the warp function. The quasi coordinate ($\hat{\phi}$) has relations with the twist (ϕ) as follows

$$\hat{\phi} = \phi - \int_0^r w'v''dx \tag{4.18}$$

where r denotes the blade radial station. By differentiating this equation, Eq. (4.19) - Eq. (4.20) can be acquired.

$$\phi' = \hat{\phi}' + w'v'' \tag{4.19}$$

$$\delta\phi' = \delta\hat{\phi}' + w'\delta v'' + v''\delta w' \tag{4.20}$$

The deformation variable u has relations with the quasi-coordinate u_e as follows

$$u' = u_e' - \frac{1}{2}(v'^2 + w'^2) \tag{4.21}$$

$$u = u_e - \frac{1}{2}\int_0^x (v'^2 + w'^2)dx \tag{4.22}$$

$$\delta u' = \delta u_e' - v'\delta v' - w'\delta w' \tag{4.23}$$

$$\delta u = \delta u_e - \int_0^x (v'\delta v' + w'\delta w')dx \tag{4.24}$$

Using Eq. (4.19) - Eq. (4.24), the strains become as follows

$$\begin{aligned}\epsilon_{xx} = u_e' - \lambda_T(\hat{\phi}'' + w''v'' + w'v''') + (\eta^2 + \zeta^2)(\theta'\hat{\phi}' + \theta'w'v'' + \frac{\hat{\phi}'^2}{2} + \frac{w'^2v''^2}{2} + \hat{\phi}'w'v'')\\ -v''[\eta cos(\theta + \hat{\phi}) - \zeta sin(\theta + \hat{\phi})] - w''[\eta sin(\theta + \hat{\phi}) + \zeta cos(\theta + \hat{\phi})]\end{aligned} \tag{4.25}$$

$$\gamma_{x\eta} = -\hat{\zeta}(\hat{\phi}' + w'v'') \tag{4.26}$$

$$\gamma_{x\zeta} = \hat{\eta}(\hat{\phi}' + w'v'') \tag{4.27}$$

The variation of strains become

$$\begin{aligned}
\delta\epsilon_{xx} = \delta u_e' &- \lambda_T(\delta\hat{\phi}'' + w''\delta v'' + v''\delta w'' + w'\delta v''' + v'''\delta w') \\
&+ (\eta^2 + \zeta^2)(\theta'\delta\hat{\phi}' + \theta' w'\delta v'' + \theta' v''\delta w' + (\hat{\phi}' + w'v'')(\delta\hat{\phi}' + w'\delta v'' + v''\delta w')) \\
&- [\eta cos(\theta + \hat{\phi}) - \zeta sin(\theta + \hat{\phi})]\delta v'' + [\eta sin(\theta + \hat{\phi}) + \zeta cos(\theta + \hat{\phi})]v''\delta\hat{\phi} \\
&- [\eta sin(\theta + \hat{\phi}) + \zeta cos(\theta + \hat{\phi})]\delta w'' - [\eta cos(\theta + \hat{\phi}) + \zeta sin(\theta + \hat{\phi})]w''\delta\hat{\phi}
\end{aligned} \tag{4.28}$$

$$\delta\gamma_{x\eta} = -\hat{\zeta}(\delta\hat{\phi}' + w'\delta v'' + v''\delta w') \tag{4.29}$$

$$\delta\gamma_{x\zeta} = \hat{\eta}(\delta\hat{\phi}' + w'\delta v'' + v''\delta w') \tag{4.30}$$

The variation of strain energy is acquired by substituting Eq. (4.28),(4.29) and (4.30) into Eq. (4.14). This equation can be nondimensionalized as follows.

$$\delta\bar{U} = \frac{\delta U}{m_0\Omega^2 R^3} = \int_0^1 (U_{u_e'}\delta u_e' + U_{v'}\delta v' + U_{w'}\delta w' + U_{v''}\delta v'' + U_{w''}\delta w'' + U_{\hat{\phi}}\delta\hat{\phi} + U_{\hat{\phi}'}\delta\hat{\phi}' + U_{\hat{\phi}''}\delta\hat{\phi}'')dx \tag{4.31}$$

where the coefficients are

$$\begin{aligned}
U_{u_e'} =& EA[u_e' + K_A^2(\theta'\hat{\phi}' + \theta' w'v'' + \frac{\hat{\phi}'^2}{2})] \\
&- EAe_A[v''(cos\theta - \hat{\phi} sin\theta) + w''(sin\theta + \hat{\phi} cos\theta]
\end{aligned} \tag{4.32}$$

$$U_{v'} = 0 \tag{4.33}$$

$$U_{w'} = (GJ + EB_1\theta'^2)\hat{\phi}'v'' + EAK_A^2\theta' v'' u_e' \tag{4.34}$$

$$
\begin{aligned}
U_{v''} = & v''[EI_z cos^2(\theta+\hat{\phi}) + EI_y sin^2(\theta+\hat{\phi})] \\
& + w''(EI_z - EI_y)cos(\theta+\hat{\phi})sin(\theta+\hat{\phi}) \\
& - EB_2\theta'\hat{\phi}cos\theta - EAe_A u_e'(cos\theta - \hat{\phi}sin\theta) + EAK_A^2 u_e' w'\theta' \\
& + (GJ + EB_1\theta'^2)\hat{\phi}'w' - EC_2\hat{\phi}''sin\theta
\end{aligned} \tag{4.35}
$$

$$
\begin{aligned}
U_{w''} = & w''[EI_z sin^2(\theta+\hat{\phi}) + EI_y cos^2(\theta+\hat{\phi})] \\
& + v''(EI_z - EI_y)cos(\theta+\hat{\phi})sin(\theta+\hat{\phi}) \\
& - EB_2\theta'\hat{\phi}sin\theta - EAe_A u_e'(sin\theta + \hat{\phi}cos\theta) + EC_2\hat{\phi}''cos\theta
\end{aligned} \tag{4.36}
$$

$$U_{\hat{\phi}} = (EI_z - EI_y)((w''^2 - v''^2)cos(\theta+\hat{\phi})sin(\theta+\hat{\phi}) + v''w''cos2(\theta+\hat{\phi})) \tag{4.37}$$

$$U_{\hat{\phi}'} = GJ(\hat{\phi}' + w'v'') + EAK_A^2(\theta' + \hat{\phi}')u_e' + EB_1\theta'^2\hat{\phi}' - EB_2\theta'(v''cos\theta + w''sin\theta) \tag{4.38}$$

$$U_{\hat{\phi}''} = EC_1\hat{\phi}'' + EC_2(w''cos\theta - v''sin\theta) \tag{4.39}$$

The following sectional properties need to be defined to express the variation of strain energy in a simple form.

$$\iint_A E d\eta d\zeta = EA \tag{4.40}$$

$$\iint_A E\eta d\eta d\zeta = EAe_A \tag{4.41}$$

$$\iint_A E\zeta^2 d\eta d\zeta = EI_y \tag{4.42}$$

$$\iint_A E\eta^2 d\eta d\zeta = EI_z \tag{4.43}$$

$$\iint_A G(\eta^2 + \zeta^2) d\eta d\zeta = GJ \tag{4.44}$$

$$\iint_A E(\eta^2+\zeta^2)d\eta d\zeta = EAK_A^2 \tag{4.45}$$

$$\iint_A E(\eta^2+\zeta^2)^2 d\eta d\zeta = EB_1 \tag{4.46}$$

$$\iint_A E\eta(\eta^2+\zeta^2)d\eta d\zeta = EB_2 \tag{4.47}$$

$$\iint_A E\lambda_T^2 d\eta d\zeta = EC_1 \tag{4.48}$$

$$\iint_A E\zeta\lambda_T d\eta d\zeta = EC_2 \tag{4.49}$$

4.1.3 Kinetic Energy

The kinetic energy of the rotor blade is calculated by using two velocities. The first one is the relative blade velocity with respect to the hub. The second one is the hub velocity itself. The hub velocity originated from fuselage motions and is ignored in this study. Let the location of a point after the beam deformation is defined by (x_1, y_1, z_1) where

$$x_1 = x + u - \lambda_T\phi' - v'(y_1 - v) - w'(z_1 - w) \tag{4.50}$$

$$y_1 = v + (y_1 - v) \tag{4.51}$$

$$z_1 = w + (z_1 - w) \tag{4.52}$$

where

$$y_1 - v = \eta cos(\theta + \hat{\phi}) - \zeta sin(\theta + \hat{\phi}) \tag{4.53}$$

$$z_1 - w = \eta sin(\theta + \hat{\phi}) + \zeta cos(\theta + \hat{\phi}) \tag{4.54}$$

The blade velocity can be expressed as

$$\vec{V} = \frac{\partial \vec{r}}{\partial t} + \vec{\Omega} \times \vec{r} \tag{4.55}$$

The rotational velocity vector $\vec{\Omega}$ is defined with precone angle of β_p with respect to the rotor shaft.

$$\vec{\Omega} = \Omega sin\beta_p \hat{i} + \Omega cos\beta_p \hat{k} \tag{4.56}$$

The time derivative of displacement is

$$\frac{\partial \vec{r}}{\partial t} = \dot{x}_1 \hat{i} + \dot{y}_1 \hat{j} + \dot{z}_1 \hat{k} \tag{4.57}$$

Using Eq. (4.56) and Eq. (4.57) in Eq. (4.55), then we have

$$\vec{V} = (\dot{x}_1 - y_1 \Omega cos\beta_p)\hat{i} + (\dot{y}_1 + x_1 \Omega cos\beta_p - z_1 \Omega sin\beta_p)\hat{j} + (\dot{z}_1 + y_1 \Omega sin\beta_p)\hat{k} \tag{4.58}$$

All velocities are nondimensionalized by $R\Omega$, and the time derivative can be converted to the azimuth angle derivative by using chain rule.

$$\dot{(\ )} = \frac{\partial(\ )}{\partial t} = \frac{\partial(\ )}{\partial \psi}\frac{\partial \psi}{\partial t} = \Omega \frac{\partial(\ )}{\partial \psi} \tag{4.59}$$

Then the variations of the velocities in nondimensionalized form become

$$\begin{aligned}\vec{V}\cdot\delta\vec{V} &= \dot{x}_1\delta\dot{x}_1 - y_1 cos\beta_p\delta\dot{x}_1 - \dot{x}_1 cos\beta_p\delta y_1 + y_1 cos^2\beta_p\delta y_1 \\ &+ \dot{y}_1\delta\dot{y}_1 + x_1 cos\beta_p\delta\dot{y}_1 - z_1 sin\beta_p\delta\dot{y}_1 + \dot{y}_1 cos\beta_p\delta x_1 + x_1 cos^2\beta_p\delta x_1 \\ &- z_1 sin\beta_p cos\beta_p\delta x_1 - \dot{y}_1 sin\beta_p\delta z_1 - x_1 cos\beta_p sin\beta_p\delta z_1 + z_1 sin^2\beta_p\delta z_1 \\ &+ \dot{z}_1\delta\dot{z}_1 + \dot{z}_1 sin\beta_p\delta y_1 + y_1 sin\beta_p\delta\dot{z}_1 + y_1 sin^2\beta_p\delta y_1\end{aligned} \tag{4.60}$$

In generalized Hamilton's principle, the kinetic energy needs to be integrated in time between t_1 and t_2. The initial and final values are set to zero. By using integration by parts, the variations of the velocities can be converted to

$$\begin{aligned}\vec{V}\cdot\delta\vec{V} &= -\ddot{x}_1\delta x_1 + 2\dot{y}_1 cos\beta_p\delta x_1 + y_1 cos^2\beta_p\delta y_1 \\ &- \ddot{y}_1\delta y_1 - 2\dot{x}_1 cos\beta_p\delta y_1 + 2\dot{z}_1 sin\beta_p\delta y_1 + x_1 cos^2\beta_p\delta x_1 \\ &- z_1 sin\beta_p cos\beta_p\delta x_1 - x_1 cos\beta_p sin\beta_p\delta z_1 + z_1 sin^2\beta_p\delta z_1 \\ &- \ddot{z}_1\delta z_1 - 2\dot{y}_1 sin\beta_p\delta z_1 + y_1 sin^2\beta_p\delta y_1\end{aligned} \tag{4.61}$$

The variation of kinetic energy in nondimensionalized form is expressed as follows

$$\frac{\delta T}{m_0\Omega^2 R^3} = \int_0^1 [\iint_A \rho\vec{V}\cdot\delta\vec{V}d\eta d\zeta]dx = \int_0^1 [\iint_A \rho(T_{x_1}\delta x_1 + T_{y_1}\delta y_1 + T_{z_1}\delta z_1)d\eta d\zeta]dx \tag{4.62}$$

where T_{x_1}, T_{x_2} and T_{x_3} are

$$T_{x_1} = -\ddot{x}_1 + 2\dot{y}_1 cos\beta_p + x_1 cos^2\beta_p - z_1 sin\beta_p cos\beta_p \tag{4.63}$$

$$T_{y_1} = -\ddot{y}_1 + y_1 cos^2\beta_p - 2\dot{x}_1 cos\beta_p + 2\dot{z}_1 sin\beta_p + y_1 sin^2\beta_p \tag{4.64}$$

$$T_{z_1} = -\ddot{z}_1 - x_1 cos\beta_p sin\beta_p + z_1 sin^2\beta_p - 2\dot{y}_1 sin\beta_p \tag{4.65}$$

Using Eq. (4.50), Eq. (4.51), and Eq. (4.52), the time derivatives of the displacement become

$$\begin{aligned}\dot{y}_1 &= \dot{v} - (\eta sin(\theta + \hat{\phi}) + \zeta cos(\theta + \hat{\phi}))\dot{\theta}_1 \\ &= \dot{v} - (z_1 - w)\dot{\theta}_1\end{aligned} \tag{4.66}$$

$$\begin{aligned}\dot{z}_1 &= \dot{w} + (\eta cos(\theta + \hat{\phi}) - \zeta sin(\theta + \hat{\phi}))\dot{\theta}_1 \\ &= \dot{w} + (y_1 - v)\dot{\theta}_1\end{aligned} \tag{4.67}$$

$$\begin{aligned}\dot{x}_1 &= \dot{u} - \lambda_T\dot{\hat{\phi}}' - \dot{v}'(y_1 - v) - v'(\dot{y}_1 - \dot{v}) - \dot{w}'(z_1 - w) - w'(\dot{z}_1 - \dot{w}) \\ &= \dot{u} - \lambda_T\dot{\hat{\phi}}' - (\dot{v}' + w'\dot{\theta}_1)(y_1 - v) + (v'\dot{\theta}_1 - \dot{w}')(z_1 - w)\end{aligned} \tag{4.68}$$

where θ_1 is $\theta + \hat{\phi}$.

The second derivatives of the displacement are

$$\ddot{y}_1 = \ddot{v} - (z_1 - w)\ddot{\theta}_1 - (y_1 - v)\dot{\theta}_1^2 \tag{4.69}$$

$$\ddot{z}_1 = \ddot{w} + (y_1 - v)\ddot{\theta}_1 - (z_1 - w)\dot{\theta}_1^2 \tag{4.70}$$

$$\begin{aligned}\ddot{x}_1 = \ddot{u} - \lambda_T\ddot{\hat{\phi}}' &- (\ddot{v}' + 2\dot{w}'\dot{\theta}_1 + w'\ddot{\theta}_1 - v'\dot{\theta}_1^2)(y_1 - v) \\ &+ (2\dot{v}'\dot{\theta}_1 + v'\ddot{\theta}_1 - \ddot{w}' + w'\dot{\theta}_1^2)(z_1 - w)\end{aligned} \tag{4.71}$$

The variations of the displacement are

$$\delta y_1 = \delta v - (z_1 - w)\delta\hat{\phi} \tag{4.72}$$

$$\delta z_1 = \delta w + (y_1 - v)\delta\hat{\phi} \tag{4.73}$$

$$\delta x_1 = \delta u - \lambda_T\delta\hat{\phi}' - (\delta v' + w'\delta\hat{\phi})(y_1 - v) + (v'\delta\hat{\phi} - \delta w')(z_1 - w) \tag{4.74}$$

Using Eq. (4.63) - Eq. (4.74) in Eq. (4.62), the variation of kinetic energy in nondimensionalized form becomes

$$\frac{\delta T}{m_0 \Omega^2 R^3} = \int_0^1 m(T_{u_e}\delta u_e + T_v \delta v + T_w \delta w + T_{v'}\delta v' + T_{w'}\delta w' + T_\phi \delta\phi + T_F)dx \tag{4.75}$$

The following sectional properties are useful to make simple expression.

$$\iint_A \rho d\eta d\zeta = m \tag{4.76}$$

$$\iint_A \rho\eta d\eta d\zeta = m e_g \tag{4.77}$$

$$\iint_A \rho\zeta^2 d\eta d\zeta = m k_{m1}^2 \tag{4.78}$$

$$\iint_A \rho\eta^2 d\eta d\zeta = m k_{m2}^2 \tag{4.79}$$

$$m k_m^2 = m k_{m1}^2 + m k_{m2}^2 \tag{4.80}$$

All the terms in Eq. (4.75) are truncated up to second order

$$T_{u_e} = -\ddot{u} + u + x + 2\dot{v} \tag{4.81}$$

The relations between u and u_e are shown in Eq. (4.21) - Eq. (4.24).

$$\begin{aligned} T_v = {} & -\ddot{v} + e_g\ddot{\theta}sin\theta + e_g cos\theta + v - \hat{\phi}sin\theta + 2\dot{w}\beta_p + 2e_g\dot{v}'cos\theta \\ & +2e_g\dot{w}'sin\theta + \ddot{\hat{\phi}}e_g sin\theta - 2\dot{u}_e + 2\int_0^x (v'\dot{v}' + w'\dot{w}')dx \end{aligned} \tag{4.82}$$

$$T_w = -\ddot{w} - e_g\ddot{\theta}cos\theta - e_g\ddot{\hat{\phi}}cos\theta - 2\dot{v}\beta_p - x\beta_p \tag{4.83}$$

$$T_{v'} = -e_g(xcos\theta - \hat{\phi}xsin\theta + 2\dot{v}cos\theta) \tag{4.84}$$

$$T_{w'} = -e_g(xsin\theta - \hat{\phi}xcos\theta + 2\dot{v}sin\theta) \tag{4.85}$$

$$\begin{aligned} T_{\hat{\phi}} = -k_m^2\ddot{\hat{\phi}} - (k_{m2}^2 - k_{m1}^2)(\hat{\phi}cos2\theta + cos\theta sin\theta) - x\beta_p e_g cos\theta \\ - ve_g sin\theta + xv'e_g sin\theta - xw'e_g cos\theta + \ddot{v}e_g sin\theta - \ddot{w}e_g cos\theta - k_m^2\ddot{\theta} \end{aligned} \tag{4.86}$$

The non variational term T_F becomes

$$T_F = -T_{u_e}\int_0^x (v'\delta v' + w'\delta w')dx \tag{4.87}$$

4.1.4 Virtual Work

The virtual work in nondimensionalized form is expressed as follows

$$\frac{\delta W}{m_0\Omega^2 R^3} = \int_0^1 (L_u^A\delta u + L_v^A\delta v + L_w^A\delta w + M_{\hat{\phi}}^A\delta\hat{\phi})dx \tag{4.88}$$

where L_u^A, L_v^A and L_w^A are the aerodynamic loads along the x, y, and z directions. $M_{\hat{\phi}}$ stands for the aerodynamic pitching moment.

4.1.5 Governing Equations

By using the Hamilton's Principle (Eq. (4.1)) and collecting the terms related with δu, δv, δw and $\delta\hat{\phi}$, the equations of motion of rotor blade can be obtained as follows.

$$\begin{aligned} EA[u_e' + K_A^2(\theta'\hat{\phi}' + \theta'w'v'' + \frac{\hat{\phi}'^2}{2})]' - EAe_A[v''(cos\theta - \hat{\phi}sin\theta) + w''(sin\theta + \hat{\phi}cos\theta)]' \\ +m(\ddot{u}_e - u_e - x - 2\dot{v}) = L_u \end{aligned} \tag{4.89}$$

$$[v''(EI_z cos^2(\theta+\hat{\phi}) + EI_y sin^2(\theta+\hat{\phi})) + w''(EI_z - EI_y)cos(\theta+\hat{\phi})sin(\theta+\hat{\phi}) - EB_2\theta'\hat{\phi}'cos\theta$$
$$-EAe_A u_e'(cos\theta - \hat{\phi}sin\theta) + EAK_A^2 u_e' w'\theta']' - m[-\ddot{v} + e_g\ddot{\theta}sin\theta + e_g cos\theta + v - \hat{\phi}sin\theta$$
$$+2\dot{w}\beta_p + 2e_g\dot{v}'cos\theta + 2e_g\dot{w}'sin\theta + \ddot{\hat{\phi}}e_g sin\theta - 2\dot{u}_e + 2\int_0^x (v'\dot{v}' + w'\dot{w}')dx]$$
$$-me_g(xcos\theta - \hat{\phi}xsin\theta + 2\dot{v}cos\theta)' + [mv'\int_x^1(-\ddot{u}_e + u_e + x + 2\dot{v}]' = L_v \tag{4.90}$$

$$[w''(EI_z sin^2(\theta+\hat{\phi}) + EI_y cos^2(\theta+\hat{\phi})) + v''(EI_z - EI_y)cos(\theta+\hat{\phi})sin(\theta+\hat{\phi}) - EB_2\theta'\hat{\phi}'sin\theta$$
$$-EAe_A u_e'(sin\theta + \hat{\phi}cos\theta) + EC_2\hat{\phi}''cos\theta]' - m[-\ddot{w} + e_g\ddot{\theta}cos\theta - \ddot{\hat{\phi}}e_g cos\theta - 2\dot{v}\beta_p - x\beta_p]$$
$$-me_g(xsin\theta + \hat{\phi}xcos\theta + 2\dot{v}sin\theta)' + [mw'\int_x^1(-\ddot{u}_e + u_e + x + 2\dot{v})]' = L_w \tag{4.91}$$

$$(w''^2 - v''^2)(EI_z - EI_y)cos(\theta+\hat{\phi})sin(\theta+\hat{\phi}) + v''w''(EI_z - EI_y)cos2(\theta+\hat{\phi})$$
$$-[GJ(\hat{\phi}' + w'v'') + EAK_A^2(\theta' + \hat{\phi}')u_e' + EB_1\theta'^2\hat{\phi}' - EB_2\theta'(v''cos\theta + w''sin\theta)]'$$
$$+[EC_1\hat{\phi}'' + EC_2(w''cos\theta - v''sin\theta)]'' - (-k_m^2\ddot{\hat{\phi}} - (k_{m2}^2 - k_{m1}^2)(\hat{\phi}cos2\theta + cos\theta sin\theta) - x\beta_p e_g cos\theta$$
$$-ve_g sin\theta + xv'e_g sin\theta - xw'e_g cos\theta + \ddot{v}e_g sin\theta - \ddot{w}e_g cos\theta - k_m^2\ddot{\theta}) = L_{\hat{\phi}} \tag{4.92}$$

4.2 Structural Finite Element Model

4.2.1 Finite Element Discretization in Space

The rotor blade is discretized into a number of beam elements. Each beam element has fifteen degrees of freedom. These degrees of freedom are distributed over five element nodes. Six degrees of freedom are used at boundary node, and they are u, v, v', w, w', and ϕ. It is also allocated two nodes for axial deflection, u, and one node for twist ϕ. Figure 4.1

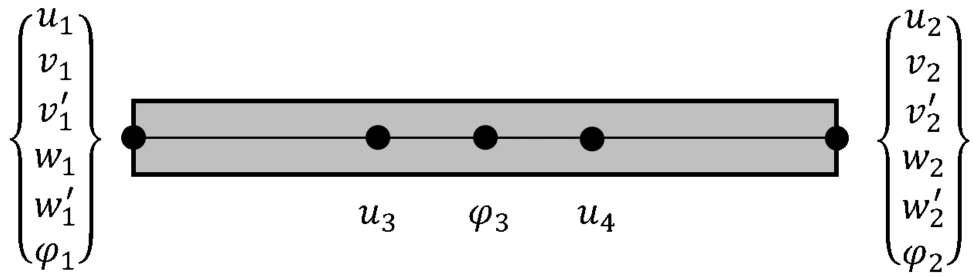

Figure 4.1: 15 degree of freedom beam element

shows a beam model with 15 degrees of freedom for each element to accommodate axial, lag-wise, bend-wise, and torsional displacements. By using the interpolation polynomials, the displacement over a beam element can be expressed in terms of elemental nodal displacement q_i. The displacement of i-th beam element is expressed as follows

$$\begin{Bmatrix} u(s) \\ v(s) \\ w(s) \\ \hat{\phi}(s) \end{Bmatrix} = \begin{pmatrix} H_u & 0 & 0 & 0 \\ 0 & H_v & 0 & 0 \\ 0 & 0 & H_w & 0 \\ 0 & 0 & 0 & H_{\hat{\phi}} \end{pmatrix} q_i \tag{4.93}$$

where $s = x/l_i$, l_i is the length of i-th beam element, q_i is the elemental nodal displacement vector.

$$q_i = \begin{Bmatrix} u_1 & u_2 & u_3 & u_4 & v_1 & v_1' & v_2 & v_2' & w_1 & w_1' & w_2 & w_2' & \hat{\phi}_1 & \hat{\phi}_2 & \hat{\phi}_3 \end{Bmatrix}^T \tag{4.94}$$

The interpolating polynomial shape functions are

$$H_u = \begin{Bmatrix} -4.5s^3 + 9s^2 - 5.5s + 1 \\ 13.5s^3 - 22.5s^2 + 9s \\ -13.5s^3 + 18s^2 - 4.5s \\ 4.5s^3 - 4.5s^2 + s \end{Bmatrix}^T \tag{4.95}$$

$$H = \begin{Bmatrix} 2s^3 - 3s^2 + 1 \\ (s^3 - 2s^2 + s)l_i \\ -2s^3 + 3s^2 \\ (s^3 - s^2)l_i \end{Bmatrix}^T \tag{4.96}$$

$$H_{\hat{\phi}} = \begin{Bmatrix} 2s^2 - 3s + 1 \\ -4s^2 + 4s \\ 2s^2 - s \end{Bmatrix}^T \tag{4.97}$$

The shape functions for flap and lead-lag deflections (Hermite Polynomials) insure the continuity of displacement and slope respectively, and the shape functions for axial and twist (Lagrange Polynomials) insure the continuity of displacement. By using finite element discretization, the second-order equation of motion of rotor blade can be expressed as

$$\mathbf{M}\ddot{q} + \mathbf{C}\dot{q} + \mathbf{K}q = \mathbf{F} \tag{4.98}$$

where $\mathbf{M}$, $\mathbf{C}$, and $\mathbf{K}$ are the mass, damping, and stiffness matrices of the system respectively. The Vector $\mathbf{F}(t)$ is the external force vector, and the vector q represents the displacements along all degrees of freedom. At this point, it is necessary to show the element mass, stiffness, damping matrices and load vector in detail. These element matrices and vector are assembled to construct the global matrices and load vector which are shown in the structural governing equation (Eq.(4.98)). The element mass, stiffness and damping matrices can be partitioned to indicate the contributions of axial deflection, lead-lag bending, flap bending and torsion as follows.

$$[M]_i = \begin{bmatrix} [M_{uu}] & [M_{uv}] & [M_{uw}] & [M_{u\phi}] \\ [M_{vu}] & [M_{vv}] & [M_{vw}] & [M_{v\phi}] \\ [M_{wu}] & [M_{wv}] & [M_{ww}] & [M_{w\phi}] \\ [M_{\phi u}] & [M_{\phi v}] & [M_{\phi w}] & [M_{\phi\phi}] \end{bmatrix} \tag{4.99}$$

$$[K]_i = \begin{bmatrix} [K_{uu}] & [K_{uv}] & [K_{uw}] & [K_{u\phi}] \\ [K_{vu}] & [K_{vv}] & [K_{vw}] & [K_{v\phi}] \\ [K_{wu}] & [K_{wv}] & [K_{ww}] & [K_{w\phi}] \\ [K_{\phi u}] & [K_{\phi v}] & [K_{\phi w}] & [K_{\phi\phi}] \end{bmatrix} \tag{4.100}$$

$$[C]_i = \begin{bmatrix} [C_{uu}] & [C_{uv}] & [C_{uw}] & [C_{u\phi}] \\ [C_{vu}] & [C_{vv}] & [C_{vw}] & [C_{v\phi}] \\ [C_{wu}] & [C_{wv}] & [C_{ww}] & [C_{w\phi}] \\ [C_{\phi u}] & [C_{\phi v}] & [C_{\phi w}] & [C_{\phi\phi}] \end{bmatrix} \tag{4.101}$$

The element mass matrix terms are expressed as

$$[M_{uu}] = \int_0^1 m\mathbf{H}_u^T\mathbf{H}_u ds \tag{4.102}$$

$$[M_{vv}] = \int_0^1 m\mathbf{H}^T\mathbf{H} ds \tag{4.103}$$

$$[M_{ww}] = \int_0^1 m\mathbf{H}^T\mathbf{H}ds \tag{4.104}$$

$$[M_{\phi\phi}] = \int_0^1 mk_m^2\mathbf{H}_{\hat{\phi}}^T\mathbf{H}_{\hat{\phi}}ds \tag{4.105}$$

$$[M_{v\phi}] = -\int_0^1 me_g\sin\theta\mathbf{H}^T\mathbf{H}_{\hat{\phi}}ds \tag{4.106}$$

$$[M_{v\phi}] = \int_0^1 me_g\cos\theta\mathbf{H}^T\mathbf{H}_{\hat{\phi}}ds \tag{4.107}$$

$$[M_{uv}] = 0 \tag{4.108}$$

$$[M_{uw}] = 0 \tag{4.109}$$

$$[M_{vw}] = 0 \tag{4.110}$$

The element stiffness matrix terms are defined as

$$[K_{uu}] = \int_0^1 EA\mathbf{H'}_u^T\mathbf{H'}_u ds \tag{4.111}$$

$$[K_{vv}] = \int_0^1 F_A\mathbf{H'}^T\mathbf{H'}ds + \int_0^1 (EI_y\sin^2\theta + EI_z\cos^2\theta)\mathbf{H''}^T\mathbf{H''}ds - \int_0^1 m\Omega^2\mathbf{H}^T\mathbf{H}ds \tag{4.112}$$

$$[K_{ww}] = \int_0^1 F_A\mathbf{H'}^T\mathbf{H'}ds + \int_0^1 (EI_z\sin^2\theta + EI_y\cos^2\theta)\mathbf{H''}^T\mathbf{H''}ds \tag{4.113}$$

$$\begin{aligned}[K_{\phi\phi}] = \int_0^1 m\Omega^2(k_{m2}^2 - k_{m1}^2)\cos 2\theta\mathbf{H}_{\hat{\phi}}^T\mathbf{H}_{\hat{\phi}}ds + \int_0^1 (GJ + EB_1\theta'^2)\mathbf{H'}_{\hat{\phi}}^T\mathbf{H'}_{\hat{\phi}}ds \\ + \int_0^1 EC_1\mathbf{H''}_{\hat{\phi}}^T\mathbf{H''}_{\hat{\phi}}ds\end{aligned} \tag{4.114}$$

$$[K_{uv}] = -\int_0^1 EAe_A\cos\theta\mathbf{H'}_u^T\mathbf{H''}ds \tag{4.115}$$

$$[K_{uw}] = -\int_0^1 EAe_A\sin\theta\mathbf{H'}_u^T\mathbf{H''}ds \tag{4.116}$$

$$[K_{u\phi}] = \int_0^1 EAk_A^2\theta' \mathbf{H'}_u^T \mathbf{H'}_{\hat{\phi}} ds \tag{4.117}$$

$$[K_{vw}] = \int_0^1 (EI_z - EI_y) \sin\theta \cos\theta \mathbf{H''}^T \mathbf{H''} ds \tag{4.118}$$

$$\begin{aligned}[K_{v\phi}] = &\int_0^1 m\Omega^2 e_g \sin\theta \mathbf{H}^T \mathbf{H}_{\hat{\phi}} ds - \int_0^1 xm\Omega^2 e_g \sin\theta \mathbf{H'}^T \mathbf{H}_{\hat{\phi}} ds \\ &- \int_0^1 EB_2\theta' cos\theta \mathbf{H''}^T \mathbf{H'}_{\hat{\phi}} ds - \int_0^1 EC_2 \sin\theta \mathbf{H''}^T \mathbf{H''}_{\hat{\phi}} ds\end{aligned} \tag{4.119}$$

$$\begin{aligned}[K_{w\phi}] = &\int_0^1 xm\Omega^2 e_g \cos\theta \mathbf{H'}^T \mathbf{H}_{\hat{\phi}} ds - \int_0^1 EB_2\theta' \sin\theta \mathbf{H''}^T \mathbf{H'}_{\hat{\phi}} ds \\ &+ \int_0^1 EC_2 \cos\theta \mathbf{H''}^T \mathbf{H''}_{\hat{\phi}} ds\end{aligned} \tag{4.120}$$

The element damping matrix terms are expressed as

$$[C_{uv}] = -\int_0^1 2m\Omega \mathbf{H}_u^T \mathbf{H} ds \tag{4.121}$$

$$[C_{vv}] = \int_0^1 2me_g\Omega \cos\theta \mathbf{H'}^T \mathbf{H} ds - \int_0^1 2me_g\Omega \cos\theta \mathbf{H}^T \mathbf{H'} ds \tag{4.122}$$

$$[C_{vw}] = -\int_0^1 2m\Omega\beta_p \mathbf{H}^T \mathbf{H} ds - \int_0^1 2me_g\Omega \sin\theta \mathbf{H}^T \mathbf{H'} ds \tag{4.123}$$

$$[C_{vu}] = -[C_{uv}] \tag{4.124}$$

$$[C_{wv}] = -[C_{vw}] \tag{4.125}$$

$$[C_{uu}] = 0 \tag{4.126}$$

$$[C_{u\phi}] = [C_{\phi u}] = 0 \tag{4.127}$$

$$[C_{v\phi}] = [C_{\phi v}] = 0 \tag{4.128}$$

$$[C_{w\phi}] = [C_{\phi w}] = 0 \tag{4.129}$$

$$[C_{ww}] = 0 \tag{4.130}$$

$$[C_{\phi\phi}] = 0 \tag{4.131}$$

The element load vector consists of two parts. The first one is contribution of the external virtual work, δW, and the second one is contribution of the variation in kinetic energy, δT. The load terms from the kinetic energy come from the inertial forces on the rotor blade (centrifugal force). The load vector contains linear and nonlinear terms. The element load vector can be expressed as

$$F_i = (F_0)_i + (F_{NL})_i \tag{4.132}$$

The linear load vector terms are defined as

$$(F_u)_0 = \int_0^1 m\Omega^2 x \mathbf{H}_u^T ds \tag{4.133}$$

$$(F_v)_0 = \int_0^1 m(\Omega^2 e_g \cos\theta + \ddot{\theta} e_g \sin\theta)\mathbf{H}^T ds - \int_0^1 m\Omega e_g \cos\theta x \mathbf{H'}^T ds \tag{4.134}$$

$$(F_w)_0 = -\int_0^1 m\Omega^2(\beta_{pc} x + \ddot{\theta} e_g \sin\theta)\mathbf{H}^T ds - \int_0^1 m\Omega e_g \sin\theta x \mathbf{H'}^T ds \tag{4.135}$$

$$(F_\phi)_0 = -\int_0^1 mk_m^2\ddot{\theta} + m\Omega^2(k_{m2}^2 - k_{m1}^2)\sin\theta\cos\theta\mathbf{H}_{\hat{\phi}}^T ds - \int_0^1 m\Omega^2\beta_{pc} e_g \cos\theta x \mathbf{H}_{\hat{\phi}}^T ds \tag{4.136}$$

The nonlinear load vector terms are expressed as

$$(F_u)_{NL} = -\int_0^1 EA(e_A(v''\hat{\phi}\sin\theta - w''\hat{\phi}\cos\theta) + k_A^2\frac{\hat{\phi}'^2}{2} + k_A^2\theta' w' v'')\mathbf{H'}_u^T ds \tag{4.137}$$

$$\begin{aligned}(F_v)_{NL} = &\int_0^1 ((EI_z - EI_y)v''\hat{\phi}\sin 2\theta - (EI_z - EI_y)w''\hat{\phi}\cos 2\theta)\mathbf{H}''^T ds \\ &- \int_0^1 EAe_A u_e'\hat{\phi}'\sin\theta\mathbf{H}''^T ds - \int_0^1 (GJ\hat{\phi}'w' + EAk_A^2\theta' w' u_e')\mathbf{H}''^T ds \\ &+ \int_0^1 (2m\int_0^x (v'\dot{v}' + w'\dot{w}')d\xi)\mathbf{H}^T ds - \int_0^1 (2v'\int_x^1 m\dot{v}d\xi)\mathbf{H}'^T ds\end{aligned} \tag{4.138}$$

$$\begin{aligned}(F_v)_{NL} = &-\int_0^1 ((EI_z - EI_y)v''\hat{\phi}\cos 2\theta - (EI_z - EI_y)w''\hat{\phi}\sin 2\theta)\mathbf{H}''^T ds \\ &+ \int_0^1 EAe_A u_e'\hat{\phi}'\cos\theta\mathbf{H}''^T ds - \int_0^1 (GJ\hat{\phi}'v'' + EAk_A^2\theta' v'' u_e')\mathbf{H}'^T ds \\ &- \int_0^1 (2w'\int_x^1 m\dot{v}d\xi)\mathbf{H}'^T ds\end{aligned} \tag{4.139}$$

$$\begin{aligned}(F_v)_{NL} = &-\int_0^1 ((EI_z - EI_y)w''^2\sin\theta\cos\theta + (EI_z - EI_y)v''w''\cos 2\theta)\mathbf{H}_{\hat{\phi}}^T ds \\ &+ \int_0^1 (EI_z - EI_y)v''^2\sin\theta\cos\theta\mathbf{H}_{\hat{\phi}}^T ds - \int_0^1 (EAk_A^2\hat{\phi}'u_e' + GJw'v'')\mathbf{H}_{\hat{\phi}}^T ds\end{aligned} \tag{4.140}$$

The second order differential equations (Eq. (4.98)) can be reduced to first-order differential equations by introducing new state vector $\boldsymbol{y}$ and coefficient matrix $\boldsymbol{A}$ and $\boldsymbol{B}$ as follows

$$\dot{\mathbf{y}} = \mathbf{A}\mathbf{y} + \mathbf{B}\mathbf{f} \tag{4.141}$$

where,

$$\mathbf{y} = \begin{Bmatrix} q \\ \dot{q} \end{Bmatrix}, \mathbf{A} = \begin{bmatrix} \mathbf{0} & \mathbf{I} \\ -\mathbf{M}^{-1}\mathbf{K} & -\mathbf{M}^{-1}\mathbf{C} \end{bmatrix}, \mathbf{B} = \begin{bmatrix} \mathbf{0} \\ \mathbf{M}^{-1} \end{bmatrix}, \mathbf{f} = \begin{bmatrix} \mathbf{0} \\ \mathbf{F} \end{bmatrix} \tag{4.142}$$

The residual of the structural equations can be defined as

$$\mathbf{S} = \dot{\mathbf{y}} - \mathbf{A}\mathbf{y} - \mathbf{B}\mathbf{f} = 0 \tag{4.143}$$

4.2.2 Structural Governing Equation in Time Spectral Form

The identical definition and approach of time spectral method in the aerodynamic system can be applied to the structural governing equations.

$$y(t) = \hat{y}_0 + \sum_{n=1}^{N_H} (\hat{y}_{cn} cos(\omega_0 nt) + \hat{y}_{sn} sin(\omega_0 nt)) \tag{4.144}$$

The structural governing equations in the time spectral form are obtained as Eq. (4.145), where the structural state vector y and the airload vector f are expanded equivalent to the fluid state vector of aerodynamic governing equations in time spectral form, as shown in Eq. (3.8).

$$\frac{d\mathbf{y_{ts}}}{d\tau} + \mathbf{D}\mathbf{y_{ts}} - \mathbf{A}\mathbf{y_{ts}} - \mathbf{B}\mathbf{f_{ts}} = 0 \tag{4.145}$$

$$\mathbf{y_{ts}} = \begin{Bmatrix} y(t_0 + \Delta t) \\ y(t_0 + 2\Delta t) \\ ... \\ y(t_0 + T) \end{Bmatrix}, \mathbf{f_{ts}} = \begin{Bmatrix} f(t_0 + \Delta t) \\ f(t_0 + 2\Delta t) \\ ... \\ f(t_0 + T) \end{Bmatrix} \tag{4.146}$$

In this approach, the aerodynamic forces are calculated from Eq. (3.11) and implemented as external forces in Eq. (4.145) for the aeroelastic system, which in turn calculates the deformations. The nodal displacements are used to update the CFD grid mesh.

4.2.3 Derivation of Spectral Matrix in Structural Governing Equation

This section describes the derivation of spectral matrix in structural governing equations in time spectral form. Once the structural governing equations are nondimensionalized, then the time derivatives are replaced by the derivatives with respect to the azimuth angle. This can be shown by using uncoupled structural governing equations, Eq.(4.147)-Eq.(4.149).

$$m\ddot{u} - EA\frac{\partial^2 u}{\partial x^2} = f_x \tag{4.147}$$

$$m\ddot{w} - EI\frac{\partial^4 w}{\partial x^4} = f_z \tag{4.148}$$

$$mk_A^2\ddot{\theta} - GJ\frac{\partial^2 \theta}{\partial x^2} = M \tag{4.149}$$

Eq.(4.147)-Eq.(4.149) are the uncoupled governing equations of axial deflection, flap bending and twist. As shown in Eq. (4.3) and Eq. (4.5), the axial coordinate x is nondimensionalized by R, and the azimuth angle is considered as nondimensionalized time.

$$\frac{m}{m_0}\frac{\partial^2 \bar{u}}{\partial \psi^2} - \frac{EA}{m_0\Omega^2 R^2}\frac{\partial^2 \bar{u}}{\partial r^2} = \frac{f_x}{m_0\Omega^2 R} \tag{4.150}$$

$$\frac{m}{m_0}\frac{\partial^2 \bar{w}}{\partial \psi^2} - \frac{EI}{m_0\Omega^2 R^4}\frac{\partial^4 \bar{w}}{\partial r^4} = \frac{f_z}{m_0\Omega^2 R} \tag{4.151}$$

$$\frac{mk_A^2}{m_0 R^2}\frac{\partial^2 \bar{\theta}}{\partial \psi^2} - \frac{GJ}{m_0\Omega^2 R^4}\frac{\partial^2 \bar{\theta}}{\partial r^2} = \frac{M}{m_0\Omega^2 R^2} \tag{4.152}$$

Eq.(4.150)-Eq.(4.152) are nondimensionalized axial, bending and twist governing equations. The derivatives with respect to the azimuth angle take the places of the time derivatives. The spectral matrix in the structural governing equations can be derived by using equivalent process in Eq. (3.17). Taking the derivative with respect to the azimuth angle gives

$$\frac{\partial p[l]}{\partial \psi_l} = \frac{\partial}{\partial \psi_l} \sum_{k=-\frac{N-1}{2}}^{\frac{N-1}{2}} P_k e^{2\pi i k t_l / T} \tag{4.153}$$

If the rotational speed,ω_0, is constant, the azimuth angle can be defined as

$$\psi = \omega_0 t = \frac{2\pi}{T} t \tag{4.154}$$

Then $2\pi t_l/T$ in Eq.(4.153) can be replaced by ψ_l, and Eq.(4.153) becomes

$$
\begin{aligned}
\frac{\partial p[l]}{\partial \psi_l} &= \frac{\partial}{\partial \psi_l} \sum_{k=-\frac{N-1}{2}}^{\frac{N-1}{2}} P_k e^{ik\psi_l} \\
&= \sum_{k=-\frac{N-1}{2}}^{\frac{N-1}{2}} ikP_k e^{ik\psi_l} \\
&= \sum_{k=-\frac{N-1}{2}}^{\frac{N-1}{2}} ik(\frac{1}{N}\sum_{j=0}^{N-1} p[j]e^{-2\pi ikt_j/T})e^{ik\psi_l} \\
&= \frac{1}{N}\sum_{k=-\frac{N-1}{2}}^{\frac{N-1}{2}}\sum_{j=0}^{N-1} ikp[j]e^{-2\pi ikt_j/T}e^{2\pi ikt_l/T} \\
&= \frac{1}{N}\sum_{k=-\frac{N-1}{2}}^{\frac{N-1}{2}}\sum_{j=0}^{N-1} ikp[j]e^{2\pi ik(t_l/T-t_j/T)} \\
&= \frac{1}{N}\sum_{k=-\frac{N-1}{2}}^{\frac{N-1}{2}}\sum_{j=0}^{N-1} ikp[j]e^{2\pi ik(l/N-j/N)} \\
&= \frac{1}{N}\sum_{k=-\frac{N-1}{2}}^{\frac{N-1}{2}}\sum_{j=0}^{N-1} ikp[j]e^{2\pi ik(l-j)/N} \\
&= \sum_{j=0}^{N-1}\left\{\frac{1}{N}\sum_{k=-\frac{N-1}{2}}^{\frac{N-1}{2}} ike^{2\pi ik(l-j)/N}\right\}p[j] \\
&= \sum_{j=0}^{N-1} D[l,j]p[j]
\end{aligned}
\tag{4.155}
$$

Eq. (4.155) shows that the derivative with respect to the azimuth angle of the discrete periodic signal, p, can be calculated by simply multiplied by D.

$$
\frac{\partial p}{\partial \psi} = Dp \tag{4.156}
$$

This section explains the reason why Eq.(4.145) has $\mathbf{Dy_{ts}}$ instead of $\omega_0\mathbf{Dy_{ts}}$.

4.2.4 Modal Reduction of the Structural Governing Equations

The FEM structural governing equations Eq. (4.98) generally involves a lot of degrees of freedom. In order to reduce computational time, the structural governing equations are converted into the normal mode form. This process helps to reduce the number of degrees of freedom and to mitigate the convergence issues by eliminating the high frequency modes. The modal transformation requires the computation of the natural frequencies and the corresponding mode shapes of rotor blade's free vibration. To make the modal analysis, the damping matrix and the external loads are excluded. Then the structural governing equations become

$$\mathbf{M}\ddot{q} + \mathbf{K}q = 0 \tag{4.157}$$

For the free vibration of rotor blade, the displacement can be assumed as

$$q = \bar{q}e^{i\omega\psi} \tag{4.158}$$

Substituting Eq. (4.158) in Eq. (4.157) gives

$$\mathbf{K}\bar{q} = \omega^2\mathbf{M}\bar{q} \tag{4.159}$$

Eq. (4.159) is the eigenvalue problem. The eigenvalues (ω^2) are real and positive, and the corresponding eigenvectors ($\mathbf{\Phi}$) are also real and orthogonal. The displacement of rotor blade are represented by a linear combination of the mode shapes ($\mathbf{\Phi}$) and the generalized coordinates (g). The rotor blade displacement vector q is approximated with n modes.

$$q = \mathbf{\Phi} g \tag{4.160}$$

where $\mathbf{\Phi}$ is an $N \times n$ matrix and g is the generalized coordinate vector. N is the global degrees of freedom of rotor blade and n is the number of modes selected to represent the rotor blade response. Applying the normal mode transformation to Eq. (4.98) results in the normal mode equations of rotor blade.

$$\bar{\mathbf{M}}\ddot{g} + \bar{\mathbf{C}}\dot{g} + \bar{\mathbf{K}}g = \bar{\mathbf{F}} \tag{4.161}$$

where

$$\begin{aligned} \bar{\mathbf{M}} &= \mathbf{\Phi}^T \mathbf{M} \mathbf{\Phi} \\ \bar{\mathbf{C}} &= \mathbf{\Phi}^T \mathbf{C} \mathbf{\Phi} \\ \bar{\mathbf{K}} &= \mathbf{\Phi}^T \mathbf{K} \mathbf{\Phi} \\ \bar{\mathbf{F}} &= \mathbf{\Phi}^T \mathbf{F} \end{aligned} \tag{4.162}$$

$\bar{\mathbf{M}}$, $\bar{\mathbf{C}}$, $\bar{\mathbf{K}}$ and $\bar{\mathbf{F}}$ are respectively the modal mass, damping, stiffness matrices and the load vector.

4.3 CFD/CA Coupled Analysis

Comprehensive analysis includes structural response analysis and coupled trim analysis. Coupled trim analysis involves calculation of the rotor controls, vehicle orientation, and rotor blade displacement such that the trim equations and the rotor blade structural equations of motion are satisfied. The satisfaction of the vehicle trim equations means that the resultant forces and moments on the vehicle, averaged over one rotor revolution, become zero [54]. The satisfaction of the rotor blade structural equations of motion means determination of the steady periodic structural deflection with a specified set of rotor control inputs. A primary assumption on the trim analysis is a steady flight condition under the helicopter operation. This requires the solution of the blade equations to converge to a periodic solution and the rotor forces satisfy the vehicle trim equations. In order to determine this correct solution, the rotor blade structural equations and the vehicle trim equations need to be solved as one coupled solution. In general, the expressions for the vehicle equilibrium condition are

$$\sum \mathbf{F} = 0 \tag{4.163}$$

where the size of $F = [F_1, ..., F_6]^T$ depends on the trim condition considered. F_1, F_2, and F_3 are, respectively, the force equilibrium residuals in the X, Y, and Z directions, and F_4, F_5, and F_6 are the rolling, pitching, and yawing moment equilibrium residuals about the center of gravity. For trim, the unknown control inputs to be determined from the equilibrium equation Eq. (4.163) are

$$\theta = [\alpha_s, \phi_s, \theta_{75}, \theta_{1c}, \theta_{1s}, \theta_{tr}]^T \tag{4.164}$$

where α_s and ϕ_s are forward and lateral shaft tilt angles, θ_{75} is the collective pitch angle at 75 percent radius, θ_{1c} and θ_{1s} are respectively the lateral and longitudinal cyclic pitch angles. The tail rotor pitch is simply a constant collective pitch input θ_{tr}. At this point, it is necessary to discuss about CFD/CA coupling process. The fluid, structural, and flight dynamics coupling is made at each pseudo time step, while all the fluid, structural and flight dynamics solutions are converged together within pseudo-time iteration process. The followings show this procedure step by step.

1) Initialize $[w_{ts}^0, y_{ts}^0, \theta_{ts}^0]$

2) Get w_{ts} from aerodynamic analysis

$$\frac{d\mathbf{w_{ts}}}{d\tau} + \omega_0 V D\mathbf{w_{ts}} + \mathbf{R_{ts}} = 0 \tag{4.165}$$

$$\mathbf{w_{ts}^{k+1}} = \mathbf{w_{ts}^{k}} + \Delta\mathbf{w_{ts}} \tag{4.166}$$

3) Use the aerodynamic force as the external force of the structural system after r sub-iterations

4) Get y_{ts}, θ_{ts} from the coupled trim analysis

$$\frac{d\mathbf{y_{ts}}}{d\tau} + D\mathbf{y_{ts}} - \mathbf{A}\mathbf{y_{ts}} - \mathbf{B}\mathbf{f_{ts}} = 0 \tag{4.167}$$

$$\mathbf{y_{ts}^{l+1}} = \mathbf{y_{ts}^{l}} + \Delta\mathbf{y_{ts}} \tag{4.168}$$

$$\mathbf{T_{ts}} = 0 \tag{4.169}$$

$$\theta_{\mathbf{ts}}^{\mathbf{l+1}} = \theta_{\mathbf{ts}}^{\mathbf{l}} + \Delta\theta_{\mathbf{ts}} \tag{4.170}$$

5) Perform interpolation to get deformation δ_j

6) Update the aerodynamic grid system

7) Repeat 2)-6) until the aerodynamic force and structural deformation are converged

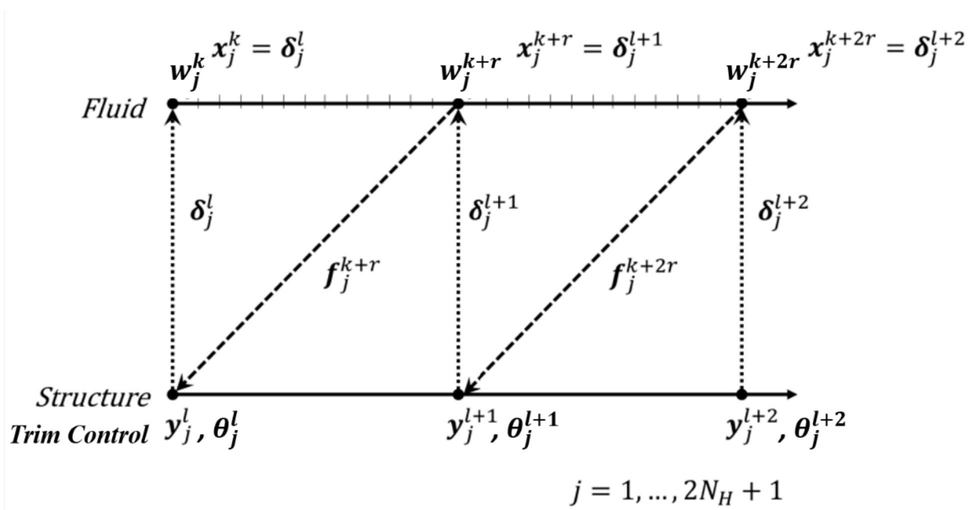

Figure 4.2: Serial staggered procedure of coupled aeroelastic analysis

Chapter 5

Coupled Sensitivity Analysis

5.1 Sensitivity Analysis

Sensitivity analysis is the process of computing derivatives of one or more quantities (outputs) with respect to one or several independent variables of interest (inputs). It is an important tool that is used across multiple disciplines, such as design optimization, uncertainty quantification, etc. Although there are various uses for sensitivity information, the main motivation is the use of sensitivity information in gradient-based optimization. A general constrained optimization problem can be expressed as

$$\begin{array}{lrr} \text{minimize} & & f(x_i) \\ \text{w.r.t} & x_i, & i = 1, 2, ..., n \\ \text{subject to} & c_j(x_i) \geq 0, & j = 1, 2, ..., m \end{array} \tag{5.1}$$

In order to solve a general constrained optimization problem using a gradient-based optimization algorithm, the sensitivities of the objective function ($\bigtriangledown f(x_i)$) and the sensitivities of all the active constraints ($\partial c_j / \partial x_i$) at the current design point should be obtained. Since the calculation of gradients is often the most costly step in the optimization cycle, using efficient methods that accurately calculate sensitivities is extremely important. There are multiple approaches adopted in practice for sensitivity analysis, the benefits and drawbacks of which shall be discussed briefly.

Most gradient-based optimizers use finite-differences for sensitivity analysis. Finite difference method is both costly and subject to inaccuracies. The computational cost of finite difference method is proportional to the number of design variables, when this number is large, sensitivity analysis is the bottleneck in the optimization cycle. Eq. 5.2 shows a forward finite difference approximation.

$$\frac{df}{dx} \approx \frac{f(x+h) - f(x)}{h} + O(h) \tag{5.2}$$

Complex step method is accurate and robust way for sensitivity calculation. The implementation of complex step method is relatively easy. However, the computational cost is also proportional to the number of design variables. Eq. 5.3 shows a complex step method.

$$\frac{df}{dx} \approx \frac{Im[f(x+ih)]}{h} + O(h^2) \tag{5.3}$$

Analytic differentiation is most accurate and efficient method available for sensitivity analysis. The function of interest can be either the objective function or any of the constraints specified in the optimization problem. In general, such function depends not only on the design variables, but also on the physical state of the system. Thus the function can be expressed as

$$f = f(x_n, y_i) \tag{5.4}$$

where x_n represents the vector of design variables and y_i is the state variable vector. For a given design variable vector x_n, the solution of the governing equations of the system yields a state vector y_i, thus establishing the dependence of the state of the system on the design variables. The governing equations can be expressed by Eq. (5.5).

$$R_k(x_n, y_i) = 0 \tag{5.5}$$

As a first step toward obtaining the derivatives, the total derivative of f can be obtained by using chain rule.

$$\frac{df}{dx_n} = \frac{\partial f}{\partial x_n} + \frac{\partial f}{\partial y_i}\frac{dy_i}{dx_n} \tag{5.6}$$

Since the governing equations must always be satisfied, the total derivative of the residuals (Eq. (5.5)) with respect to any design variable must also be zero.

$$\frac{dR_k}{dx_n} = \frac{\partial R_k}{\partial x_n} + \frac{\partial R_k}{\partial y_i}\frac{dy_i}{dx_n} = 0 \tag{5.7}$$

Eq.(5.7) provides the means for computing the total sensitivity of the state variables(y_i) with respect to the design variables(x_n). By rearranging Eq.(5.7), $\frac{dy_i}{dx_n}$ can be expressed as

$$\frac{dy_i}{dx_n} = -[\frac{\partial R_k}{\partial y_i}]^{-1}\frac{\partial R_k}{\partial x_n} \tag{5.8}$$

By substituting $\frac{dy_i}{dx_n}$, the total derivative Eq.(5.6) becomes

$$\frac{df}{dx_n} = \frac{\partial f}{\partial x_n} - \frac{\partial f}{\partial y_i}[\frac{\partial R_k}{\partial y_i}]^{-1}\frac{\partial R_k}{\partial x_n} \tag{5.9}$$

The approach where $\frac{dy_i}{dx_n}$ is first calculated by using Eq.(5.8) and then the result is substituted in the expression for the total derivative (Eq.(5.9)) is called the direct analytic method. There is an alternative option for computing the total derivative $\frac{df}{dx_n}$ in Eq.(5.9). This approach is called as adjoint method, so it is semi-analytic method. By introducing new adjoint vector

ψ_k $(= -\frac{\partial f}{\partial y_i}[\frac{\partial R_k}{\partial y_i}]^{-1})$, the adjoint equation is obtained.

$$\frac{\partial R_k}{\partial y_i}\psi_k = -\frac{\partial f}{\partial y_i} \tag{5.10}$$

Once the adjoint vector ψ_k is obtained, the total derivative of the function of interests can be calculated as follow

$$\frac{df}{dx_n} = \frac{\partial f}{\partial x_n} + \psi_k \frac{\partial R_k}{\partial x_n} \tag{5.11}$$

In contrast with the direct analytic method, the adjoint vector does not depend on the design variables (x_n), but instead depends on the function of interest (f). Therefore, if the number of design variables is greater than the number of functions, the adjoint method is computationally more efficient. Otherwise, if the number of functions to be differentiated is greater than the number of design variables, the direct analytic method would be a better choice. The details of adjoint method are discussed in next section. Automatic differentiation, also known as computational differentiation or algorithmic differentiation, is a popular approach based on the systematic application of the differentiation chain rule to computer programs. Although this approach is as accurate as an analytic method, it is potentially much easier to implement since this can be done automatically. This method is based on the application of the chain rule of differentiation to each operation in the program flow. The derivatives given by chain rule can be propagated forward or backward. Fig. 5.1 summarize the methods for computing derivatives.

5.2 Coupled Adjoint-based Sensitivity Analysis

In this study, coupled adjoint-based sensitivity analysis is carried out to get the gradient information that will be used in shape optimization. The sensitivities of objective function

Monolithic	Finite Difference	$\frac{df}{dx}=\frac{f(x+h)-f(x)}{h}+O(h)$
	Complex Step	$\frac{df}{dx}=\frac{Im[f(x+ih)]}{h}+O(h^2)$
Analytic	Direct	$\frac{df}{dx_n}=\frac{\partial f}{\partial x_n}-\frac{\partial f}{\partial y_i}\overbrace{[\frac{\partial R_k}{\partial y_i}]^{-1}\frac{\partial R_k}{\partial x_n}}^{-dy_i/dx_n}$
	Adjoint	
Automatic Differentiation	Forward	
	Backward	

Figure 5.1: Sensitivity Analysis Methods

and constraints are computed with respect to design variables which characterize the shape of rotor blade. As discussed in the Introduction chapter, the sensitivity analysis is performed using the adjoint method, and the adjoint formulation for gradient computation for current problem is derived. The design problem to be solved in this study is the optimization problem of minimizing the objective function, I, with a number of design variables, b, while satisfying a set of constraints. The objective function (I) depends on the flow state, w, the structural state, y, and the fluid mesh state, x.

$$\begin{aligned} \text{minimize} \quad & \boldsymbol{I}(w,y,x,b) \\ \text{subject to} \quad & \boldsymbol{R}(w,y,x,b)=0 \\ & \boldsymbol{S}(w,y,x,b)=0 \end{aligned} \tag{5.12}$$

Where the constraints R and S represent the time-spectral form of the fluid governing equations and the rotor blade structural equations of motion. The sensitivities of the objective with respect to the design inputs can be computed by using the chain rule.

$$\frac{dI}{db} = \frac{\partial I}{\partial b} + \frac{\partial I}{\partial w}\frac{\partial w}{\partial b} + \frac{\partial I}{\partial y}\frac{\partial y}{\partial b} + \frac{\partial I}{\partial x}\frac{\partial x}{\partial b} \tag{5.13}$$

Similarly, considering the fluid, structural state equations and the trim equations, these equations are also dependent on the same state, control inputs, and design variables. The total derivatives of the state equations and trim equations can be calculated.

$$\begin{aligned} \frac{dR(w,y,x,b)}{db} &= \frac{\partial R}{\partial b} + \frac{\partial R}{\partial w}\frac{\partial w}{\partial b} + \frac{\partial R}{\partial y}\frac{\partial y}{\partial b} + \frac{\partial R}{\partial x}\frac{\partial x}{\partial b} = 0 \\ \frac{dS(w,y,x,b)}{db} &= \frac{\partial S}{\partial b} + \frac{\partial S}{\partial w}\frac{\partial w}{\partial b} + \frac{\partial S}{\partial y}\frac{\partial y}{\partial b} + \frac{\partial S}{\partial x}\frac{\partial x}{\partial b} = 0 \end{aligned} \tag{5.14}$$

However, irrespective of the design variables, the residuals of the state equations and the trim equations must be equal to zero, as they are the governing equations. Thus, their total derivatives with respect to the design variable should remain zero. The total derivatives can then be multiplied by each of adjoint vector elements and added to the sensitivities of the objective function, as expressed in Eq. (5.15).

$$\begin{gathered} \frac{dI}{db} = \frac{\partial I}{\partial b} + \frac{\partial I}{\partial w}\frac{\partial w}{\partial b} + \frac{\partial I}{\partial y}\frac{\partial y}{\partial b} + \frac{\partial I}{\partial x}\frac{\partial x}{\partial b} + \psi_a^T\left(\frac{\partial R}{\partial b} + \frac{\partial R}{\partial w}\frac{\partial w}{\partial b} + \frac{\partial R}{\partial y}\frac{\partial y}{\partial b} + \frac{\partial R}{\partial x}\frac{\partial x}{\partial b}\right) \\ +\phi_a^T\left(\frac{\partial S}{\partial b} + \frac{\partial S}{\partial w}\frac{\partial w}{\partial b} + \frac{\partial S}{\partial y}\frac{\partial y}{\partial b} + \frac{\partial S}{\partial x}\frac{\partial x}{\partial b}\right) \end{gathered} \tag{5.15}$$

Rearranging the terms and bringing the state sensitivity terms together,

$$\begin{gathered} \frac{dI}{db} = \frac{\partial I}{\partial b} + \psi_a^T\frac{\partial R}{\partial b} + \phi_a^T\frac{\partial S}{\partial b} + \left(\frac{\partial I}{\partial w} + \psi_a^T\frac{\partial R}{\partial w} + \phi_a^T\frac{\partial S}{\partial w}\right)\frac{\partial w}{\partial b} \\ + \left(\frac{\partial I}{\partial y} + \psi_a^T\frac{\partial R}{\partial y} + \phi_a^T\frac{\partial S}{\partial y}\right)\frac{\partial y}{\partial b} + \left(\frac{\partial I}{\partial x} + \psi_a^T\frac{\partial R}{\partial x} + \phi_a^T\frac{\partial S}{\partial x}\right)\frac{\partial x}{\partial b} \end{gathered} \tag{5.16}$$

All the terms stated in Eq. (5.16) can be computed without solving the entire problem again, apart from $\partial w/\partial b$ and $\partial y/\partial b$. The change in the aerodynamic and structural state cannot be calculated without solving the FSI problem that drives the residuals goes to zero. The dependence of the objective function gradient on the sensitivity of the state can be avoided by setting the terms within the brackets to zero, giving the adjoint equation as written in Eq. (5.17).

$$\begin{bmatrix} \frac{\partial R}{\partial w} & \frac{\partial R}{\partial y} \\ \frac{\partial S}{\partial w} & \frac{\partial S}{\partial y} \end{bmatrix}^T \begin{Bmatrix} \psi_a \\ \phi_a \end{Bmatrix} = - \begin{Bmatrix} \frac{\partial I}{\partial w} \\ \frac{\partial I}{\partial y} \end{Bmatrix} \tag{5.17}$$

Then, the objective function sensitivity can be calculated by using the adjoint variable vectors from Eq. (5.17).

$$\frac{dI}{db} = \frac{\partial I}{\partial b} + \psi_a^T \frac{\partial R}{\partial b} + \phi_a^T \frac{\partial S}{\partial b} + \left(\frac{\partial I}{\partial x} + \psi_a^T \frac{\partial R}{\partial x} + \phi_a^T \frac{\partial S}{\partial x} \right) \frac{\partial x}{\partial b} \tag{5.18}$$

5.3 Adjoint Jacobian Matrix

In order to compute the sensitivity by using the adjoint method, it is required to find the adjoint Jacobian matrix first. For this, all the block Jacobians involving the coupled adjoint matrix need to be computed and assembled. Each block Jacobian will be addressed term by term for detail. Since the time spectral formulation has been applied, all the state equations, state variables, and trim control inputs are considered simultaneously in the Jacobian formulation. The state equations at a certain time instance will not depend onto the states at another time instance. Therefore, $\partial R/\partial w$ has the diagonal form shown in Eq. (5.20), where the Jacobian has both spectral parts and standard parts, and the standard part is a block Jacobian, where the subscript denotes the time instance. The computation of the fluid Jacobian at each time instance is well discussed in literature. More details of the fluid Jacobian can be found in the work of Lee. Ref.[55]

$$\frac{dR}{dw} = \frac{\partial}{\partial w}\left(\omega D w + R_{ts}\right) = \omega D + \frac{dR_{ts}}{dw} \tag{5.19}$$

$$\frac{dR_{ts}}{dw} = \begin{bmatrix} \frac{\partial R_1}{\partial w_1} & 0 & 0 & 0 \\ 0 & \frac{\partial R_2}{\partial w_2} & 0 & 0 \\ 0 & 0 & \ddots & 0 \\ 0 & 0 & 0 & \frac{\partial R_N}{\partial w_N} \end{bmatrix} \tag{5.20}$$

where N is the number of time instances. The structural Jacobian has the same structure as that of the fluid Jacobian. In fact, the structural state, given by Eq. (4.145), can be seen as a linear function of the structural state. Therefore, the structural block Jacobian is expressed as shown in Eq. (5.21)-(5.23).

$$\frac{dS}{dy} = \frac{\partial}{\partial y}\left(\omega D y + S_{ts}\right) = \omega D + \frac{dS_{ts}}{dy} \tag{5.21}$$

$$\frac{dS_{ts}}{dy} = \begin{bmatrix} \frac{\partial S_1}{\partial y_1} & 0 & 0 & 0 \\ 0 & \frac{\partial S_2}{\partial y_2} & 0 & 0 \\ 0 & 0 & \ddots & 0 \\ 0 & 0 & 0 & \frac{\partial S_N}{\partial y_N} \end{bmatrix} \tag{5.22}$$

$$\frac{dS_1}{dy_1} = A = \begin{bmatrix} 0 & I \\ -M^{-1}K & -M^{-1}C \end{bmatrix} \tag{5.23}$$

On the other hand, calculating the cross Jacobians $\partial R/\partial y$, and $\partial S/\partial w$ are not as simple as the two Jacobians previously discussed. The state equations are not explicitly a function of the other state variables. However, the state equations are affected by the each other states through the FSI coupling. For example, considering the spatially discretized form of the fluid residuals (for each cell), given by Eq.(5.24), it can be seen that the residual also depends on the cell face area projections (Δs_x) along with the fluid state.

$$R = \sum_{j=1}^{nfaces} F_j(w)\Delta s_{xj} \tag{5.24}$$

Hence, for the first off diagonal block Jacobian, $\partial R/\partial y$, a change in the structural state, deflection, would perturb the surface mesh (x_s) along the wetted boundary, which in turn would perturb the volume mesh (x_v). The perturbed volume mesh will perturb the mesh metrics (s_x) which would affect the fluid residual. Hence, the block Jacobian is computed as shown in Eq. (5.25).

$$\frac{\partial R}{\partial y} = \frac{\partial R}{\partial s_x}\frac{\partial s_x}{\partial x_v}\frac{\partial x_v}{\partial x_s}\frac{\partial x_s}{\partial y} \tag{5.25}$$

Similarly, the other off diagonal block Jacobian, $\partial S/\partial w$, can be calculated. In this case, the structural residuals would only get impacted by the fluid state through the aerodynamic force term. Only the surface elements of the fluid mesh would impact the structural residuals, as only they contribute in computing the aerodynamic force. Hence, $\partial S/\partial w$ would be sparse and is calculated as shown in Eq. (5.26).

$$\frac{\partial S}{\partial w} = \frac{\partial S}{\partial f}\frac{\partial f}{\partial p}\frac{\partial p}{\partial w} \tag{5.26}$$

The structural residual,S, is defined in Eq. (4.143). Differentiation of Eq. (4.143) with respect to external force shows that

$$\frac{\partial S}{\partial f} = -\mathbf{B} \tag{5.27}$$

The external force,f, can be calculated by integrating pressure on the rotor blade surface.

$$f = \iint_S p \, dS \tag{5.28}$$

Thus, the partial derivative, $\partial f/\partial p$, is the surface normal area vector for each surface element.

$$\frac{\partial f}{\partial p} = d\vec{S} \tag{5.29}$$

Pressure can be expressed by using fluid state variable,w.

$$p = (\gamma - 1)\left(w_5 - \frac{1}{2w_1}\left(w_2^2 + w_3^2 + w_4^2\right)\right), w = \begin{Bmatrix} w_1 \\ w_2 \\ w_3 \\ w_4 \\ w_5 \end{Bmatrix} = \begin{Bmatrix} \rho \\ \rho u \\ \rho v \\ \rho w \\ \rho E \end{Bmatrix} \tag{5.30}$$

The partial derivative, $\partial p/\partial w$, can be calculated by differentiating Eq. (5.30) one by one.

$$\delta p = (\gamma - 1)\left(\delta w_5 + \frac{1}{2w_1^2}\left(w_2^2 + w_3^2 + w_4^2\right)\delta w_1 - \frac{1}{w_1}\left(w_2 \delta w_2 + w_3 \delta w_3 + w_4 \delta w_4\right)\right) \tag{5.31}$$

The calculation of $\partial S/\partial w$ requires interpolation transfer matrix between CFD and structural node.

Chapter 6

Validation and Coupled FSI Analysis

With the framework for the time spectral FSI analysis and its sensitivity analysis using the adjoint method being established in the previous sections, the method is applied to the helicopter rotor blade. The final goal of this work is to use the time spectral method to predict the performance of the rotor blade and use that information to carry out coupled adjoint based sensitivity analysis. The representative UH-60A like geometry rotor blade based on the work in Ref. [49] has been chosen as there is a wide range of experimental and computational data in different reports which serves well for the validation studies.

6.1 Validation of Rotor Flow Analysis

Using the time spectral approach can save the computational cost and make the coupling process more efficient comparing to the conventional time accurate approach. The application of the time spectral approach has been validated for rotor flows in Choi's work [46, 47, 48, 49]. Several flight conditions of UH-60 (high speed forward flight, low speed forward flight, and dynamic stall cases) have been used for test cases. The results from the high speed forward flight case, C8534, are shown here for the validation purpose. The conventional comprehensive analysis code with lifting line theory and free wake model cannot capture the advancing side transonic flow and corresponding structural deformations, while CFD coupling with CA plays a key role in improving pitching moment and vibration prediction. High fidelity

CFD analysis seems to be a critical tool for rotor design in high speed forward flight condition [21, 56]. The time spectral analysis is coupled with a rotorcraft comprehensive analysis tool, UMARC. The UMARC supplies the structural dynamic rotor blade model, the flight dynamic model, and the airload gradient which is needed for delta method. The computational mesh is shown in Fig. 6.1. Fig 6.2 shows the pressure distributions on the blade

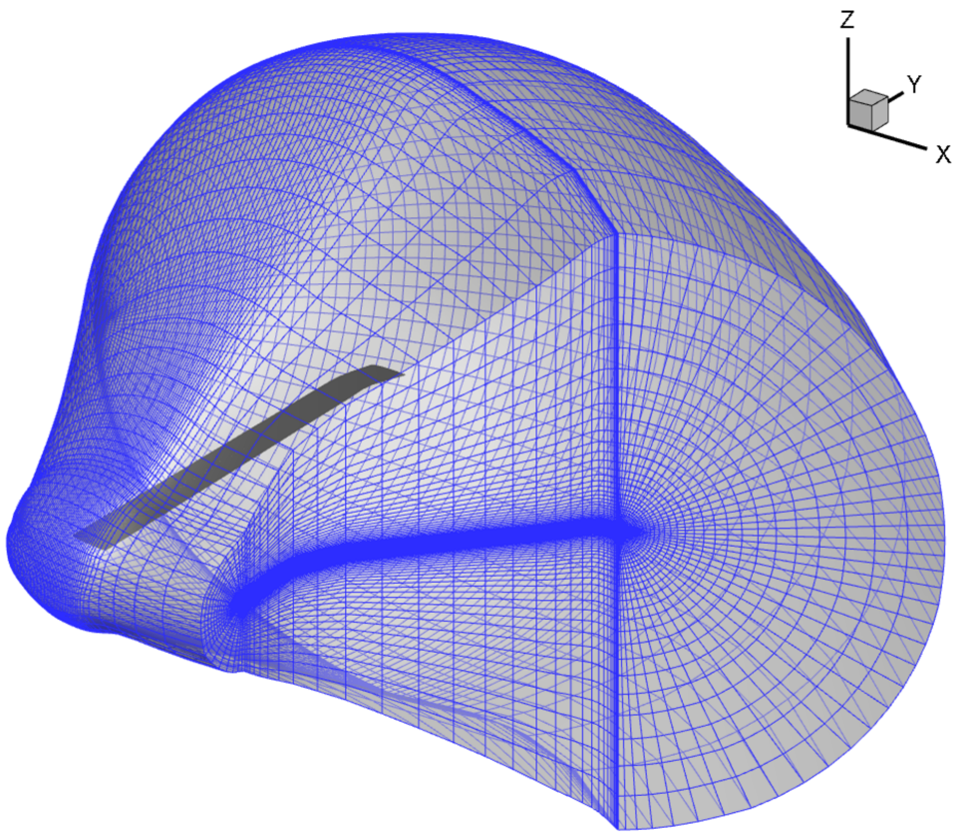

Figure 6.1: Single Bladed CFD Mesh

surfaces. The computed sectional normal forces are plotted in Figure 6.3. Also, they are compared with flight test data. The test data come from the U.S.Army/NASA-Ames UH-60A Black Hawk Airloads Program [57, 58]. The comprehensive set of flight test data from the UH-60A Airloads Program has been used as benchmark to validate rotor analysis and

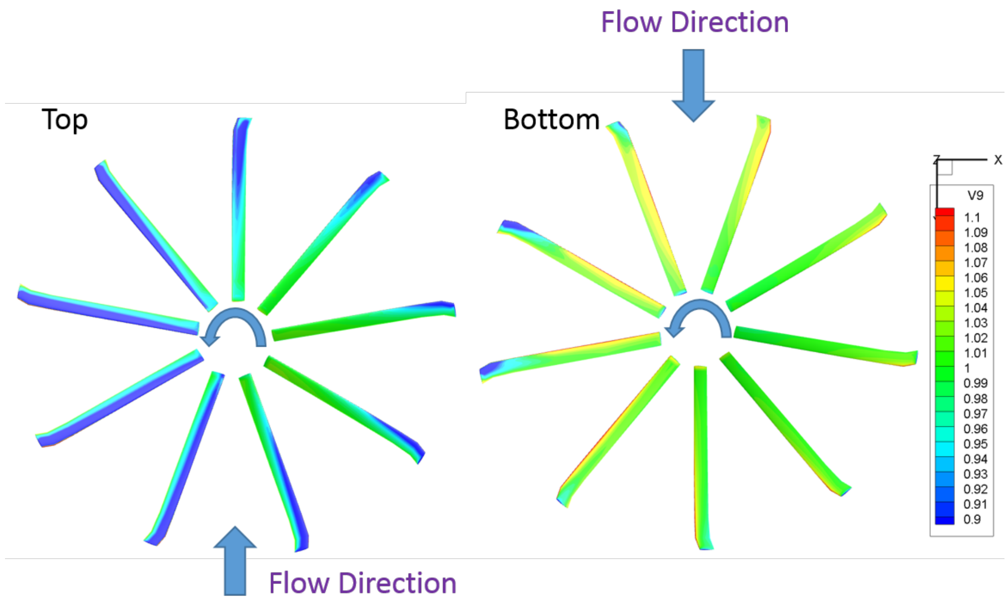

Figure 6.2: Blade Surface Pressure Contours

refine the rotor structural dynamics in UMARC. Comparison between time spectral and time accurate method shows good agreement, and both results match reasonably well with flight test measured data.

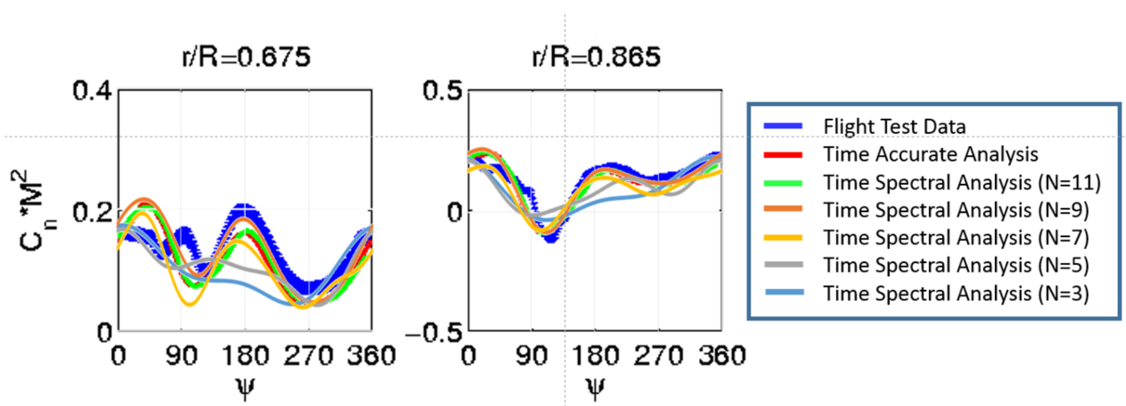

Figure 6.3: Measured and predicted normal force in high speed flight condition(C8534)

6.2 Validation of Rotor Blade Motion Analysis

In order to validate the rotor blade structural model, coupled trim analysis is performed with the high speed flight condition C8534. Coupled trim analysis involves calculation of the rotor controls, vehicle orientation, and rotor blade deformation such that the trim equations and the blade response equations are satisfied. The satisfaction of the trim equations means that the resultant forces and moments on the vehicle, averaged over one rotor revolution, become zero [6]. The air loads from the CFD calculation in previous section are used as an input of coupled trim analysis. The CFD air loads are used as correction over the air loads calculated by the lifting line theory model in UMARC. In this procedure, called the delta method, the comprehensive analysis supplies the air load sensitivities to blade deformations which provide aerodynamic damping during convergence [54]. Fig. 6.4 shows the vehicle equilibrium residuals and convergence. In this case, the convergence criteria are satisfied in 32 iterations. The changes of 6 control inputs and disc loading over the coupled trim iterations are shown in Fig. 6.5. The test data used in the present study are from Flight85 of the UH-60A Black Hawk Air Loads Program [59]. Flight 85 is a steady level flight and corresponds to a nominal vehicle weight coefficient, C_w/σ, of 0.08. For example, counter 34 data corresponds to high speed forward flight (155 kts).

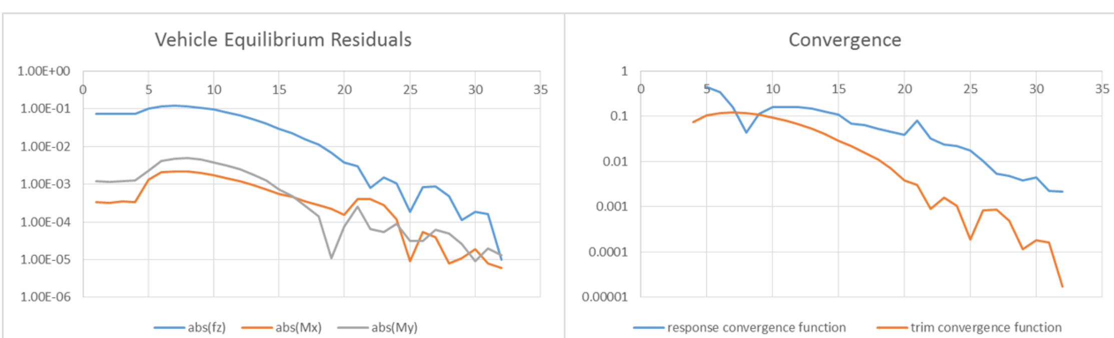

Figure 6.4: Vehicle Equilibrium Residuals and Convergence

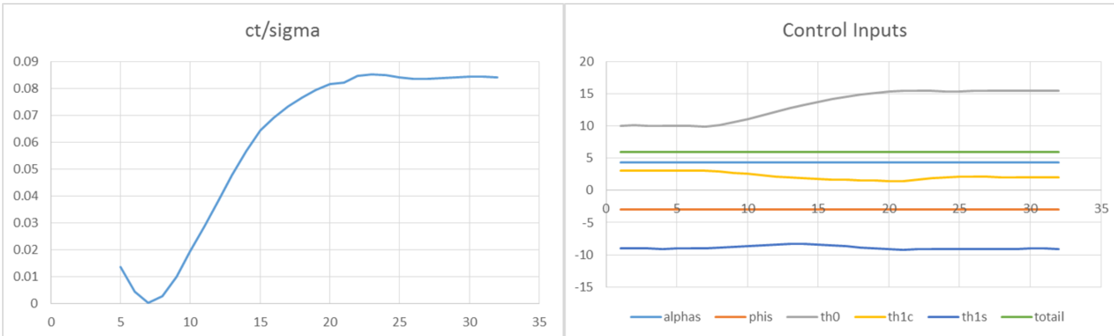

Figure 6.5: Disc Loading and Control Inputs

6.3 CFD/CA Coupled FSI Analysis

In this section, CFD is coupled with the Comprehensive Analysis (UMARC) to predict the deformation and the air loads on the rotor blade. In loose coupling, air loads are used to compute the rotor blade deformation. As a first step, lifting line theory is used to generate air loads on the rotor blade surface. By using this initial guess, the iterative coupled trim analysis calculates the rotor control inputs, vehicle orientations, and blade deformation that satisfy the trim equations and the blade response equations. Then these control inputs and deformation are used to update CFD grid mesh. With the modified mesh, CFD calculation is performed to predict the air flow around the rotor blade. By integrating pressure over the blade surface, the air load distribution on the surface of the rotor blade can be generated. The distribution of air load is again used as an input for coupled trim analysis. This step requires a proper interpolation between aero nodes and structural nodes. This whole process is repeated until the converged solution is obtained. Fig 6.6 gives a schematic of framework for this process. Figs. 6.7, 6.8, and 6.9 show how the aero coefficients change through coupled CFD-Comprehensive Analysis iterations. This analysis results in a converged solution in 8 iterations. The light blue solid line shows the first iteration results which come from the CFD analysis using the structural deformation of comprehensive analysis. This first comprehensive analysis is performed using a rough

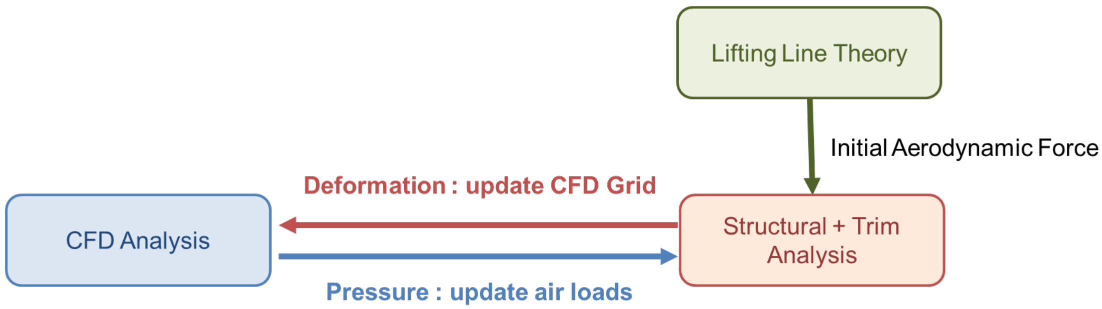

Figure 6.6: Process of CFD-Comprehensive Analysis

estimate of air load by lifting line theory. The second step (orange solid line) is calculated using delta method, which utilizes the difference between CFD and lifting line theory air loads. This process is repeated until the solution is converged. Fig. 6.10 is the convergence plot of this process.

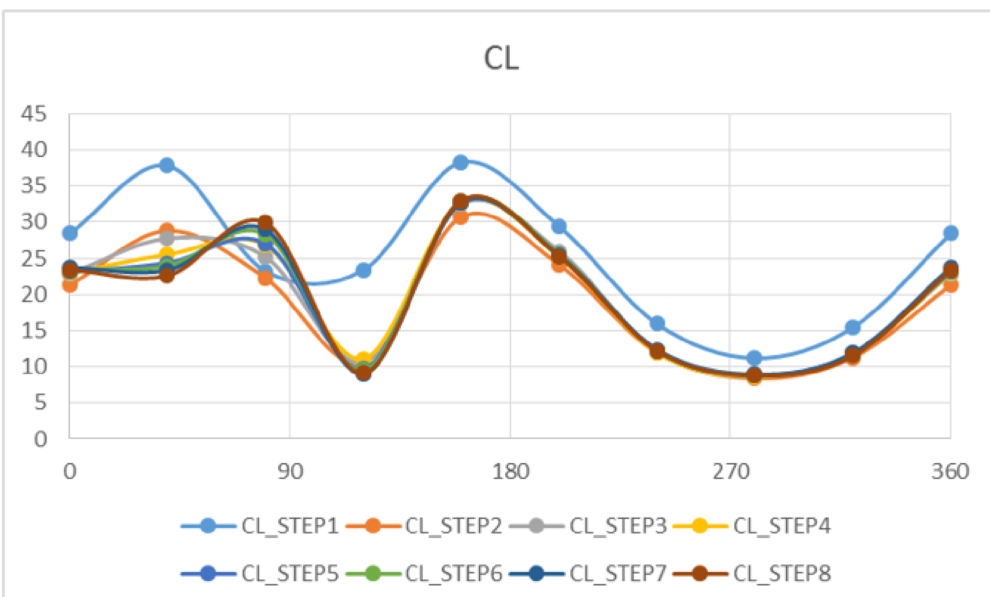

Figure 6.7: CFD-Comprehensive Analysis Results: C_L

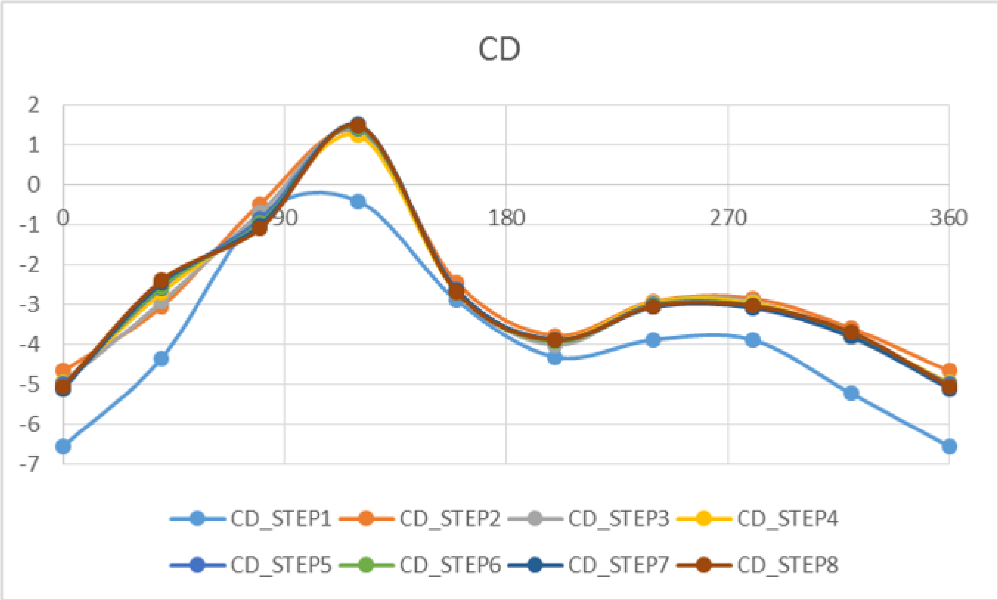

Figure 6.8: CFD-Comprehensive Analysis Results: C_D

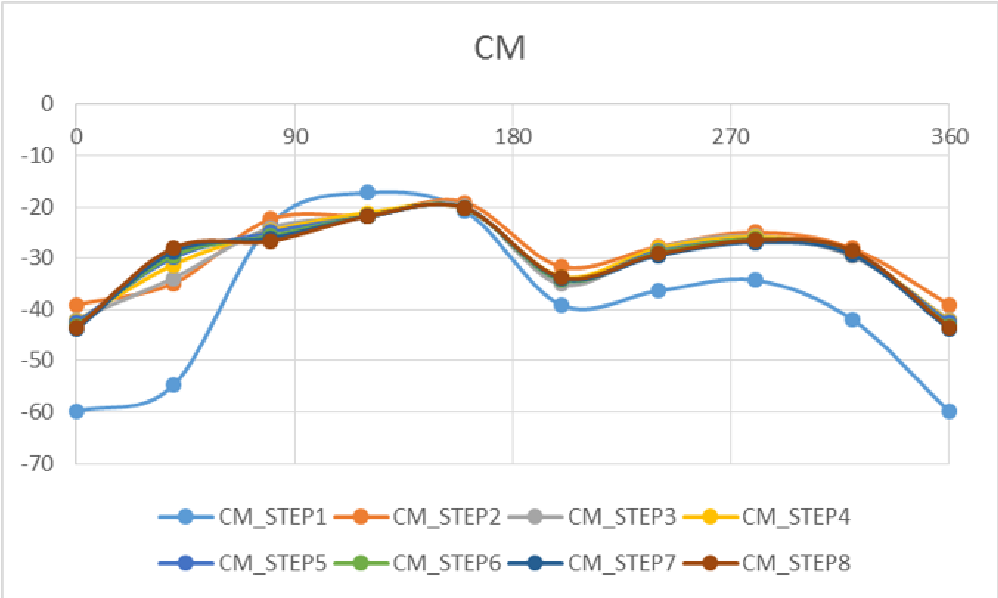

Figure 6.9: CFD-Comprehensive Analysis Results: C_M

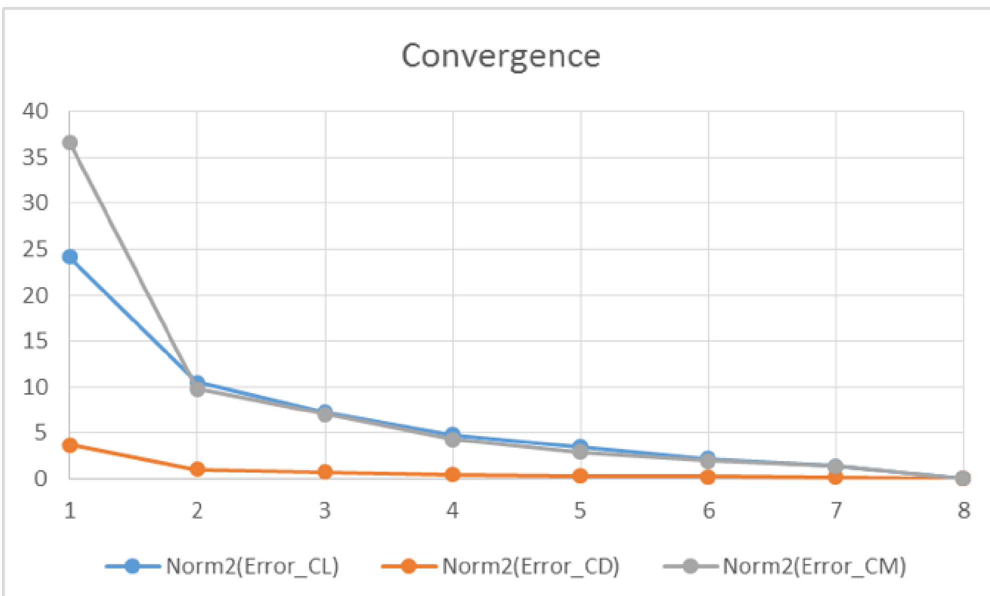

Figure 6.10: Convergence of CFD-Comprehensive Analysis

Chapter 7

Sensitivity Analysis Results

7.1 Design Problem Definition

Although shape optimization of rotor blade is not performed in this study, it is necessary to define the design problem for sensitivity analysis purpose. The objective of shape optimization problem can be minimizing the rotor torque. And the thrust level is required to be equal to or greater than the initial value. This condition can be enforced as a nonlinear constraint. Design variables are properly chosen to change the shape of the airfoil sections along the span. The airfoil shape at the 9 radial locations along the span-wise direction is perturbed by an application of Hicks-Henne bump functions. At each airfoil section, 10 bump functions are employed with the maximum bump location fixed at a designated location. The amplitudes of the bump are used as the design variables. The airfoil shapes between design locations are linearly interpolated. A total of 90 design variables are used to change the shape of the rotor blade. The maximum size of bump function is limited so that the mesh generator can make the geometry change. Fig. 7.1 shows the locations of the design variables on the rotor blade surface. Fig. 7.2 shows the rotor blade shape changes when three different size bumps are applied. delP is the design parameter which specifies the height of bump.

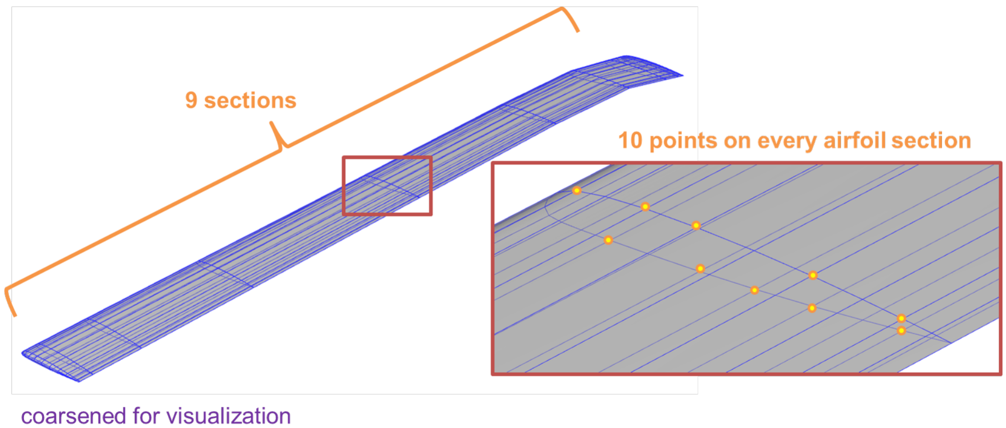

Figure 7.1: The Locations of Design Variables

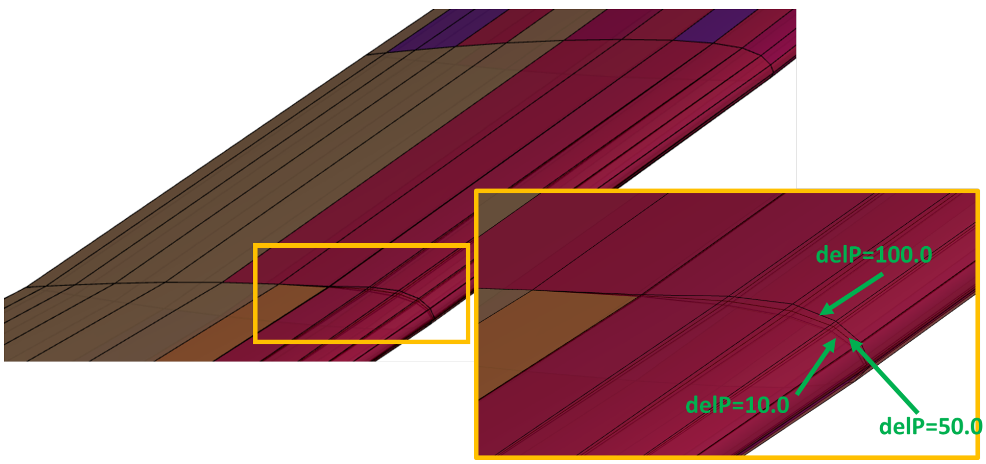

Figure 7.2: The shape changes of rotor blade with different size bumps

7.2 Aerodynamics only Sensitivity Analysis

In Section 6.3, the converged CFD-Comprehensive analysis solution is obtained. It means that the fluid and the structural states are known under a given flight condition. With these fluid and structural states, the sensitivity analysis is performed. This section shows aerodynamics only sensitivity analysis results. The contributions of the structural deformation are not included in this sensitivity analysis. Flow solutions of the time-spectral computation are used to get the values of objective function and constraints. Calculated fluid state is used as an input of the discrete adjoint solver to compute the adjoint solution. Aerodynamics only adjoint solver becomes Eq. (7.1).

$$\left[\frac{\partial R}{\partial w}\right]^T \psi_a = -\frac{\partial I}{\partial w} \tag{7.1}$$

The total derivatives of the objective with respect to the design variables are calculated via vector operations using the adjoint parameters (ψ) as in Eq. (7.2).

$$\frac{dI}{db} = \frac{\partial I}{\partial b} + \psi_a^T \frac{\partial R}{\partial b} \tag{7.2}$$

Figs.7.3 shows the locations of rotor blades at each time instance and the corresponding azimuth angles. The rotor blade at first time instance is located on top of the picture and it corresponds to zero azimuth angle. At this time, the rotor blade is aligned with the y-axis which has the same direction with free stream velocity. The rotor blade rotates in counter clock wise direction. So, the rotor blade at second time instance is located at 40 degrees. A rotor blade moving in the same direction as the vehicle is called the advancing blade, and the blade moving in the opposite direction is called the retreating blade. In the advancing side, the rotational speed is added to the free stream velocity. On the contrary, the relative speed is the difference in velocity between those two in the retreating side. The rotor blades from 2 to 5 located in advancing side, and blades at 6 to 9 are in retreating side. Figs.7.4, and 7.5 show the aerodynamics only sensitivity analysis results. Sensitivity analysis shows that the both objectives (lift and drag) are more sensitive to the design variables in the advancing side, and the location of peak is constant. Fig.7.6 shows the location of this most sensitive point in the airfoil section. This point is located on the upper surface near the leading edge.

In order to validate adjoint sensitivity analysis, sensitivity with respect to one design variable (the 72nd design variable) is calculated by using Finite Difference Method (FDM) and compared. The 72nd design variable corresponds to the peak in the Figs.7.4, and 7.5.

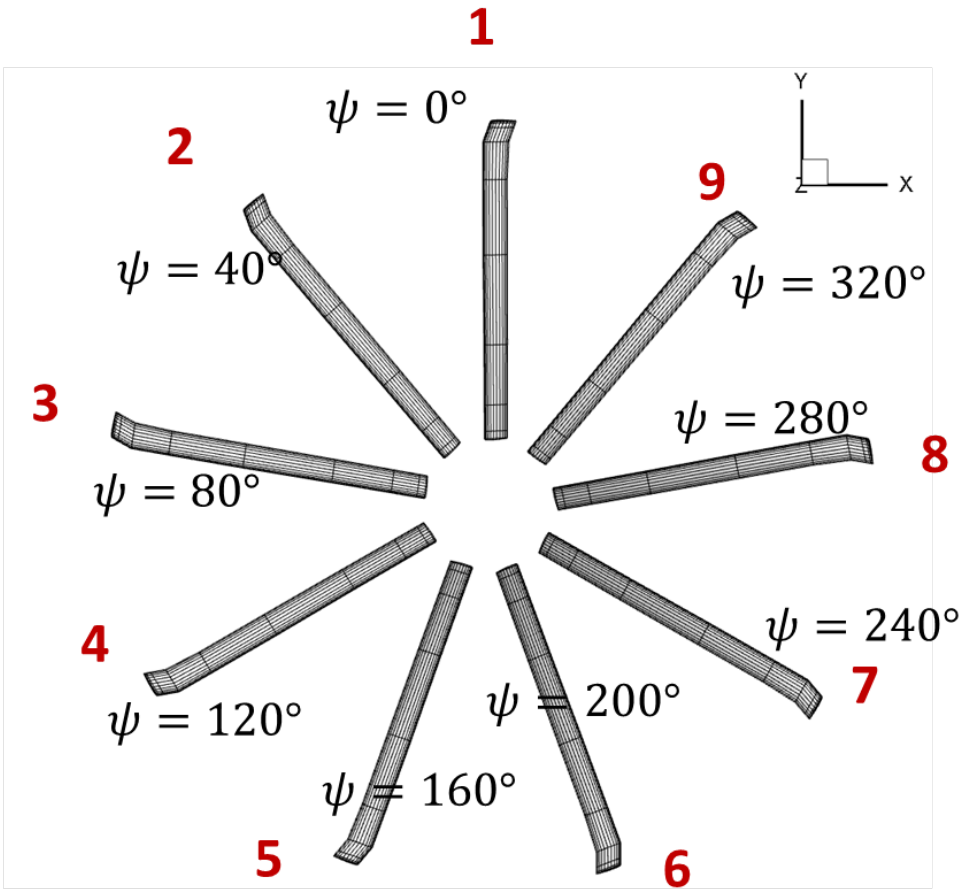

Figure 7.3: The locations of rotor blade at each time instance

Fig.7.7 shows the location of bump which is used as the 72nd design variable. Assuming that the perturbation (the height of bump function) is sufficiently small, the approximation of the first derivative of objective function can be calculated by difference between objective values with baseline and perturbed geometry. The difference needs to be divided by the magnitude of perturbation to get the sensitivity. Figs.7.8, and 7.9 show the comparison between adjoint and FDM sensitivities at 9 time instances. The comparison between two sensitivities show good agreements overall, even with presence of small discrepancies. The light blue lines show the partial derivatives of objective function with respect to the design variables, i.e. $\frac{\partial I}{\partial b}$. Partial derivative of a function of several variables is its derivative with respect to one

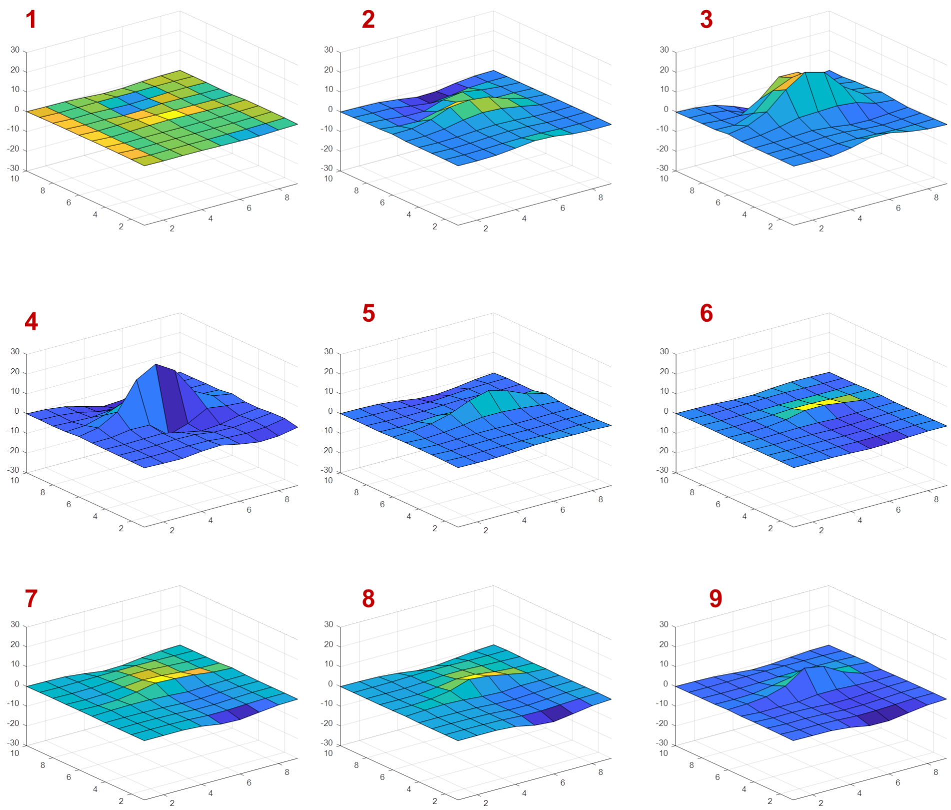

Figure 7.4: Sensitivity Analysis Result (Objective I=Drag)

of those variables, with others held constant. In this case, the $\frac{\partial I}{\partial b}$ include only the effect of the shape changes due to the design variable (bump function), such as change in surface area vectors, whereas the flow state is fixed. The difference between the partial derivatives($\frac{\partial I}{\partial b}$) and the total derivatives ($\frac{dI}{db}$) can be explained by the change of flow state, and it can be mathematically expressed as $\frac{\partial I}{\partial w}\frac{\partial w}{\partial b}$ term in Eq. (4.2). The $\frac{\partial w}{\partial b}$ is hard to calculate and inefficient in terms of computational cost. Here, adjoint method calculates equivalent $\psi_a^T\frac{\partial R}{\partial b}$ term instead of $\frac{\partial I}{\partial w}\frac{\partial w}{\partial b}$.

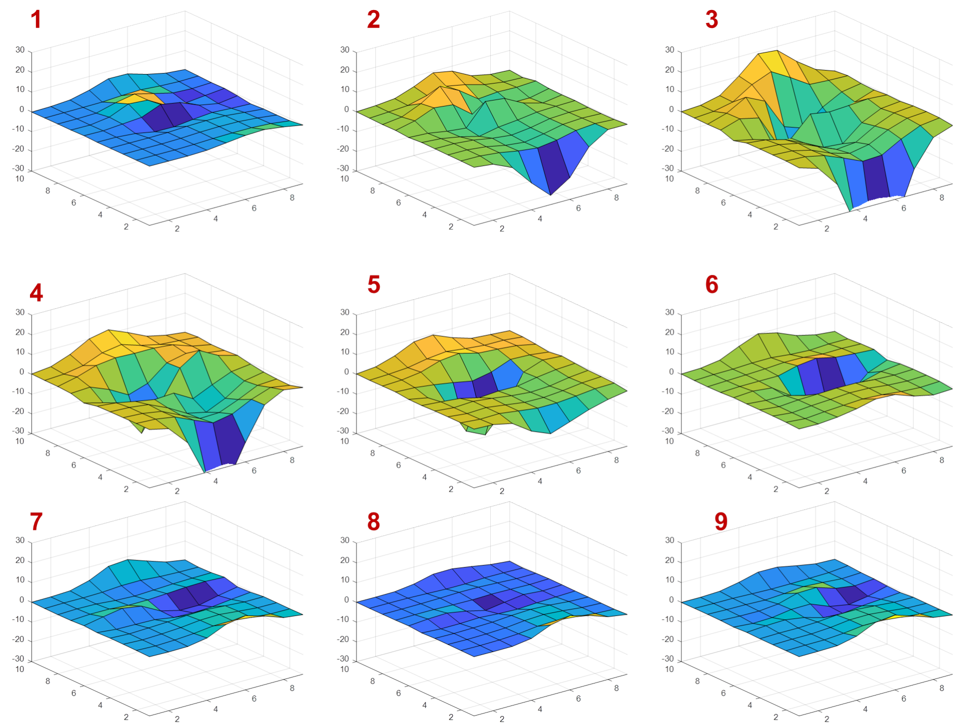

Figure 7.5: Sensitivity Analysis Result (Objective I=Lift)

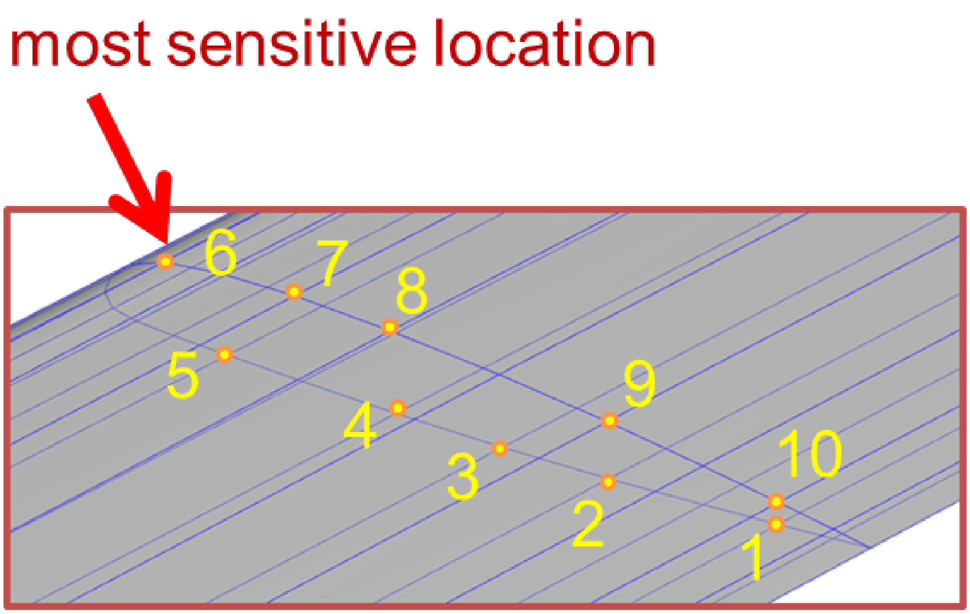

Figure 7.6: Location of Sensitive Point in Airfoil Section)

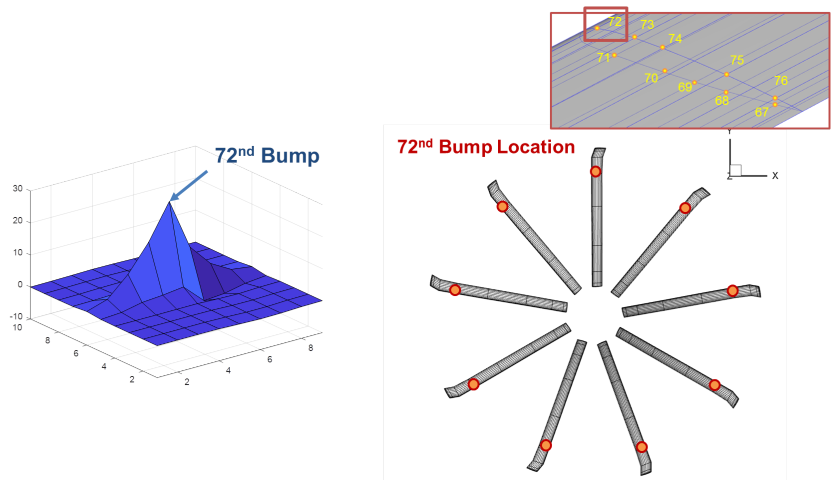

Figure 7.7: The location of 72nd design variable

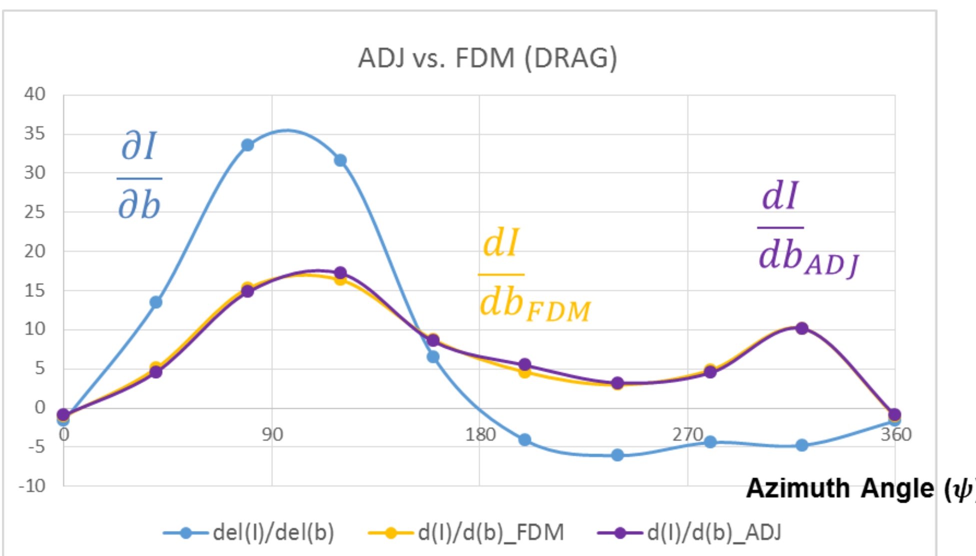

Figure 7.8: Comparison between ADJ and FDM Sensitivities (DRAG)

7.3 Sensitivity Analysis using Finite Difference Method

This section describes the sensitivity analysis using a finite difference method (FDM) that is compared with the adjoint sensitivity analysis in the previous section. The finite difference method is a numerical method for solving differential equations by approximating the

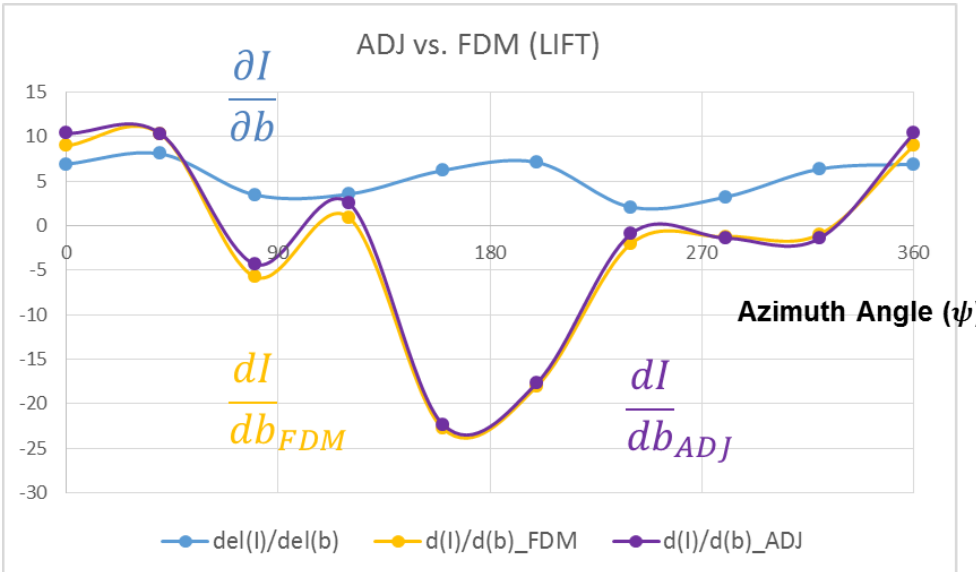

Figure 7.9: Comparison between ADJ and FDM Sensitivities (LIFT)

derivatives with finite differences. The error in FDM solution is defined as the difference between the approximation and the exact solution. The two sources of error in finite difference method are round-off error, the loss of precision due to computer rounding of decimal digits, and truncation error or discretization error that comes from approximating an infinite sum of series by a finite sum. FDM requires step size study to find optimal size of step between two sources of error. Small step size is always helpful to reduce the truncation error but it can cause the round-off error. In this study, the optimal size of bump needs to be determined. At first, 8 different sizes of bump are tested to figure out how much they affect the sensitivities of lift, drag, and pitching moment with 3 time instances. Fig.7.10 shows the convergence of lift, drag and pitching moment with three time instances with respect to the bump size. Y axis shows the sensitivity of lift, drag and moment, and X axis represents the size of bump. delP is the parameter that specifies the maximum height of the bump function, it varies from 0.125 to 10 in log scale. Drag sensitivity at the 1st time instance (CD1) shows different pattern from the other 8 curves. This can be explained by round-off error. All 8 sensitivities in CD1 show very small differences between them. The limit on the number of

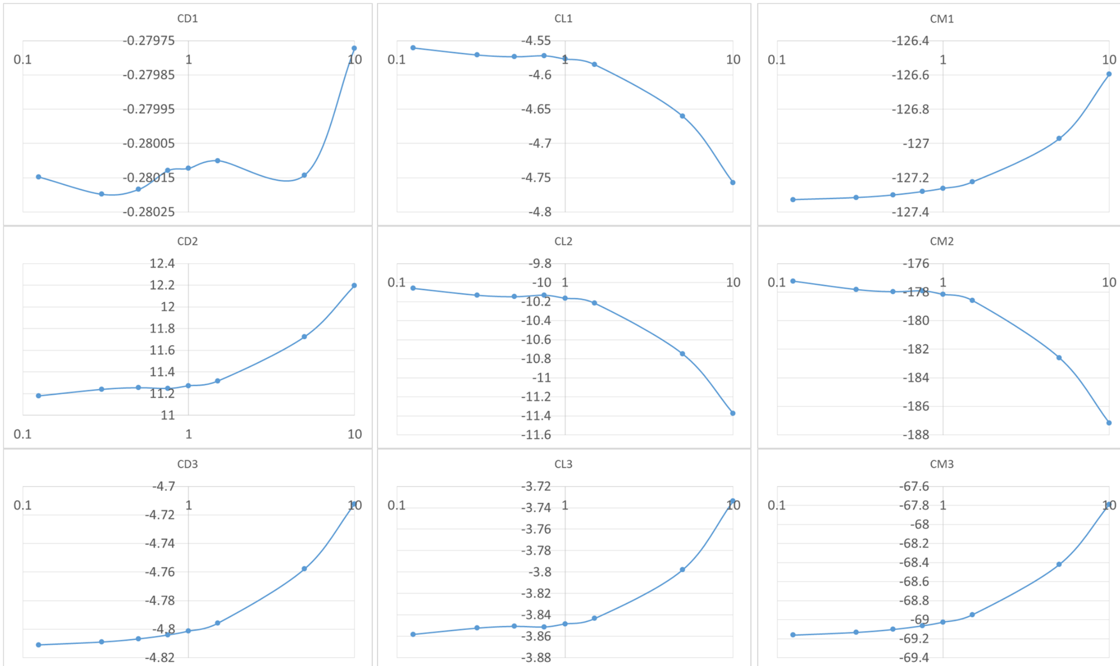

Figure 7.10: Step size study (3 time instances)

digits could be the reason of this pattern. As a result, this step size study shows that all the sensitivities are converged around delP = 1.0. Fig.7.11 and 7.12 show how the sensitivities

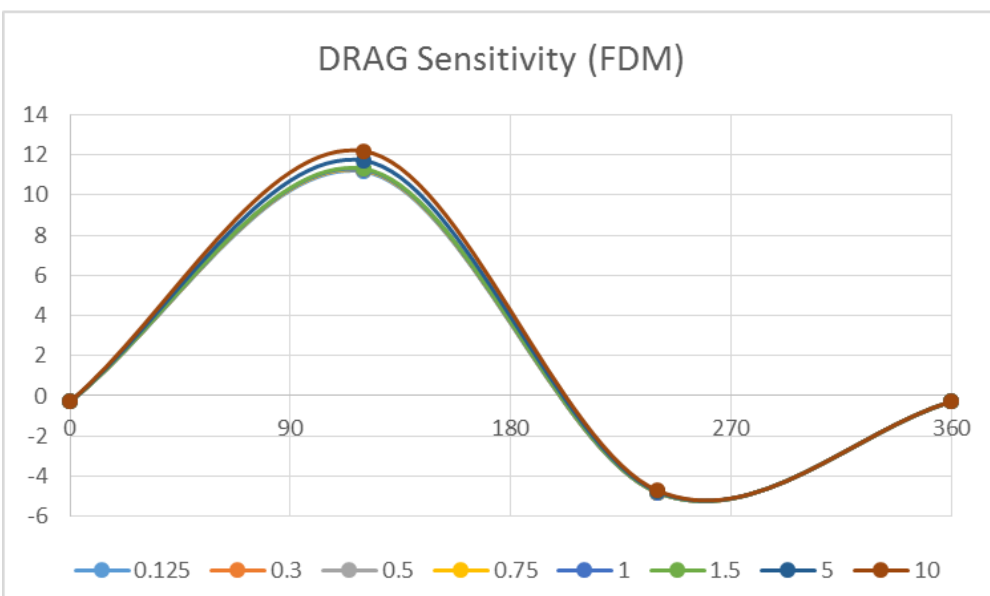

Figure 7.11: Step size study (3 time instances: DRAG)

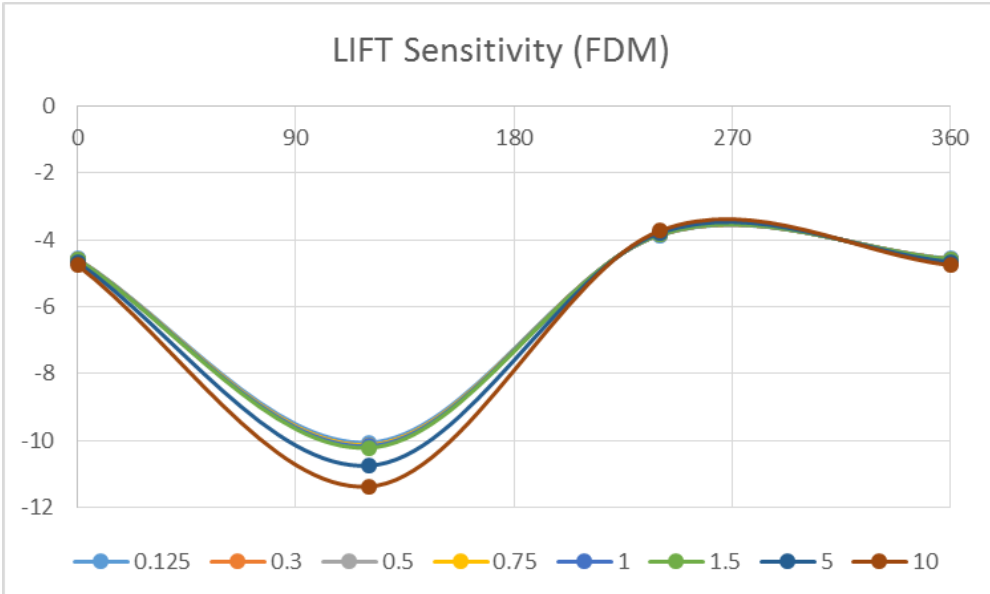

Figure 7.12: Step size study (3 time instances: LIFT)

of drag and lift along the azimuth angle change with different bump sizes. Y axis shows the sensitivity of lift and drag, and X axis represents the azimuth angle. All the curves are moving toward the smallest bump size curve (delP=0.125) as the bump size decreases. In order to check the effect of the number of time instances on the sensitivity, similar step size studies are made with a number of 9 time instances and 11 time instances. Eight different sizes of bumps are used to check the convergence of the sensitivity with respect to the bump size. Fig.7.13 - 7.15 show the lift, drag and pitching moment sensitivities with respect to the bump sizes from finite difference sensitivity analysis using 9 time instances. Again, delP=1.0 shows good enough convergence. Fig.7.16 and 7.17 show the drag and lift sensitivities along the azimuth angle. All curves fall on top of each other. The size of bump has very small effect on the drag and lift sensitivities based on 9 time instances calculation compared to the sensitivity calculation with 3 time instances. Figs.7.18 and 7.19 show the comparisons of the drag and lift sensitivities from finite difference sensitivity analysis between 3,9 and 11 time instances. The grey line (3 nTS) is much different from the others. This indicates that

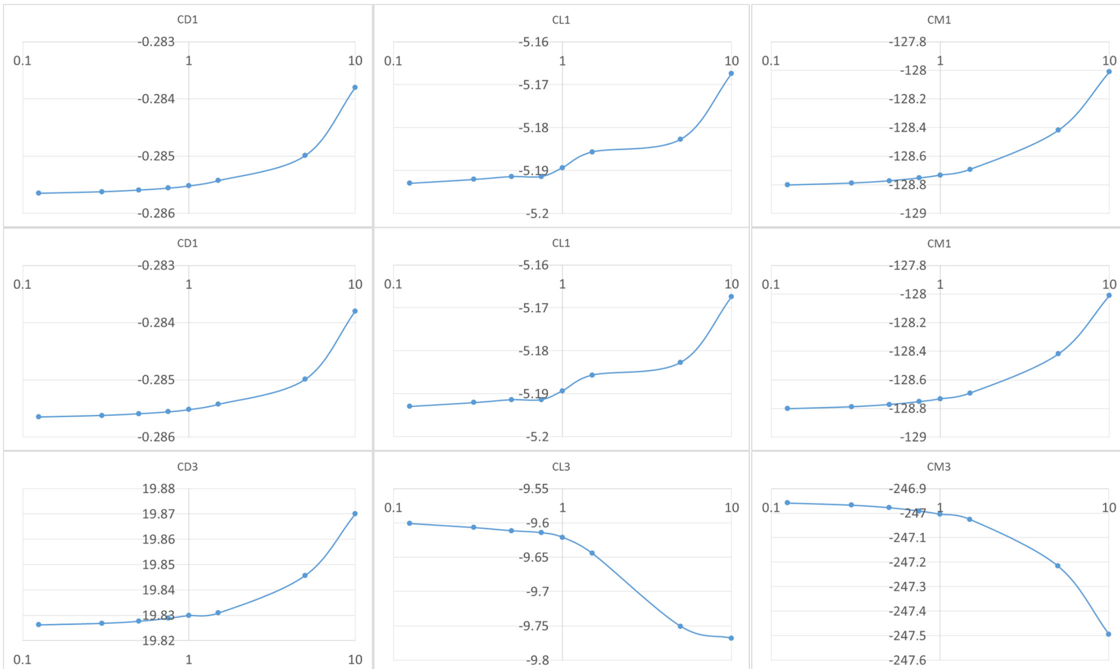

Figure 7.13: Step size study (9 time instances: 1-3)

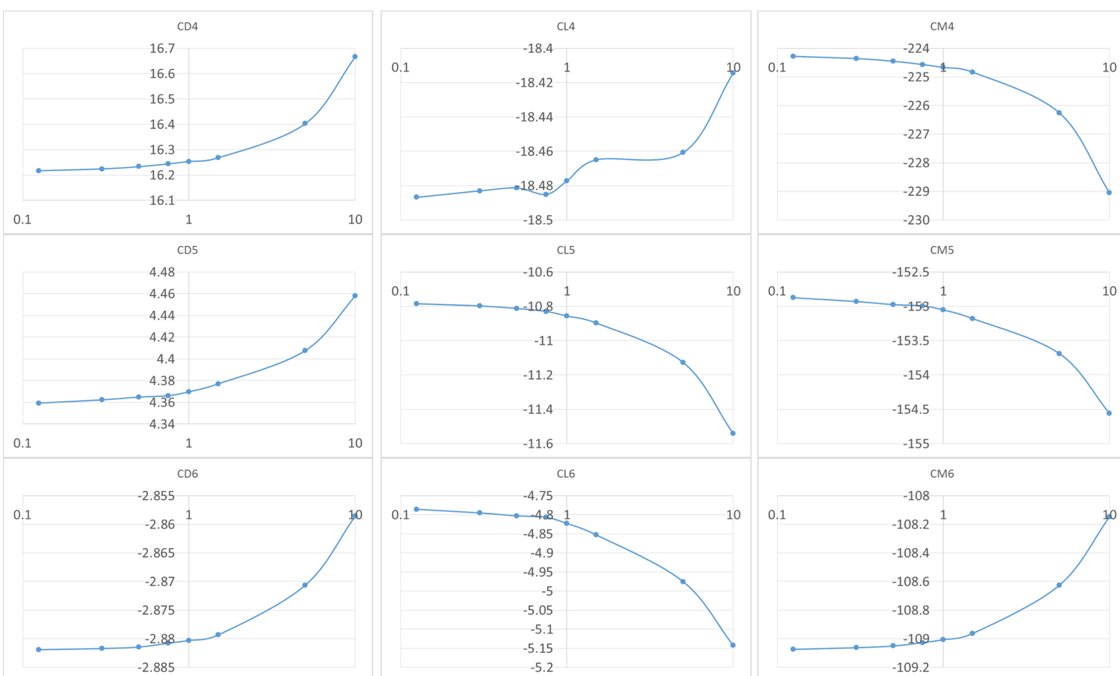

Figure 7.14: Step size study (9 time instances: 4-6)

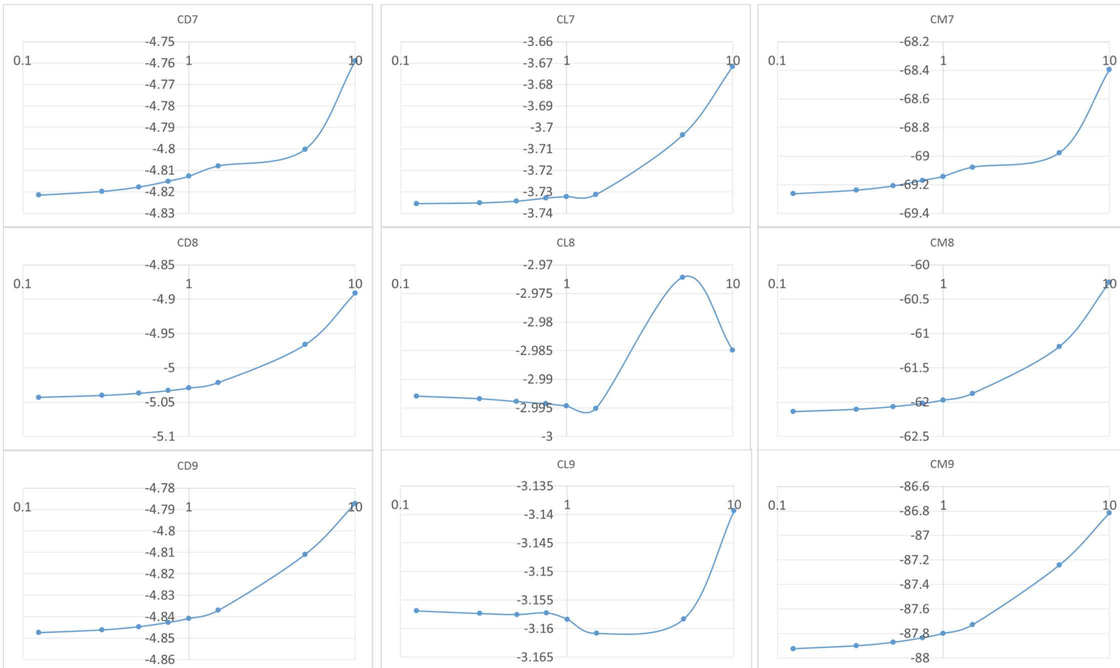

Figure 7.15: Step size study (9 time instances: 7-9)

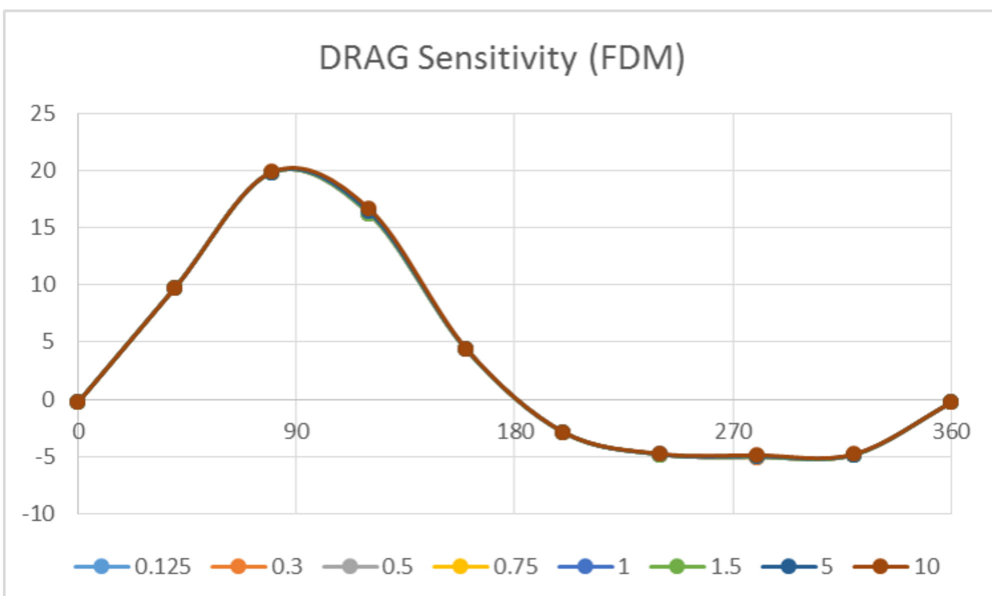

Figure 7.16: Step size study (9 time instances: DRAG)

the calculation with 3 time instances is not good enough to simulate the motion of rotor blades and to achieve exact sensitivities. For drag, the orange line (9 nTS) and the blue line

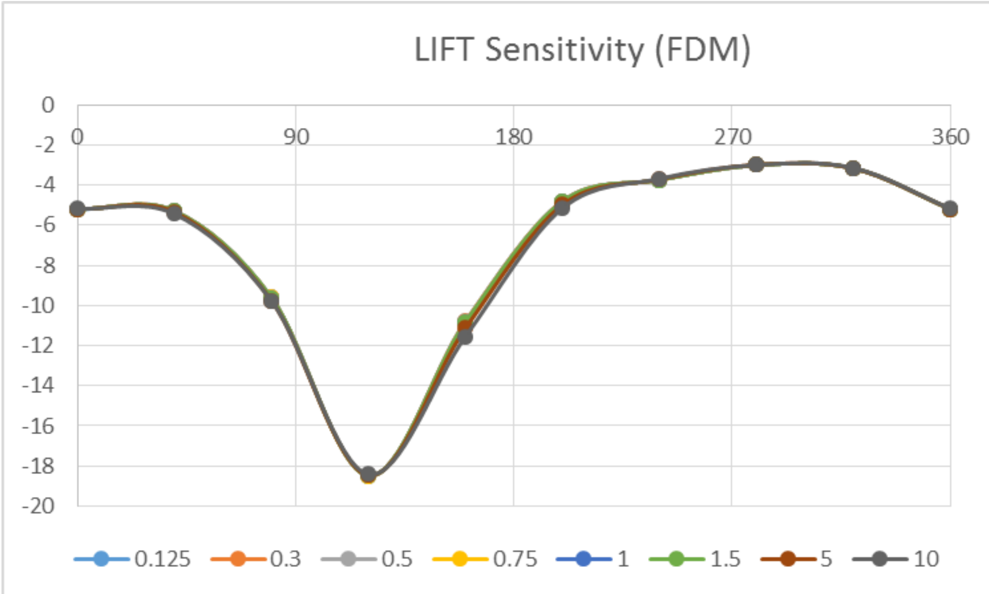

Figure 7.17: Step size study (9 time instances: LIFT)

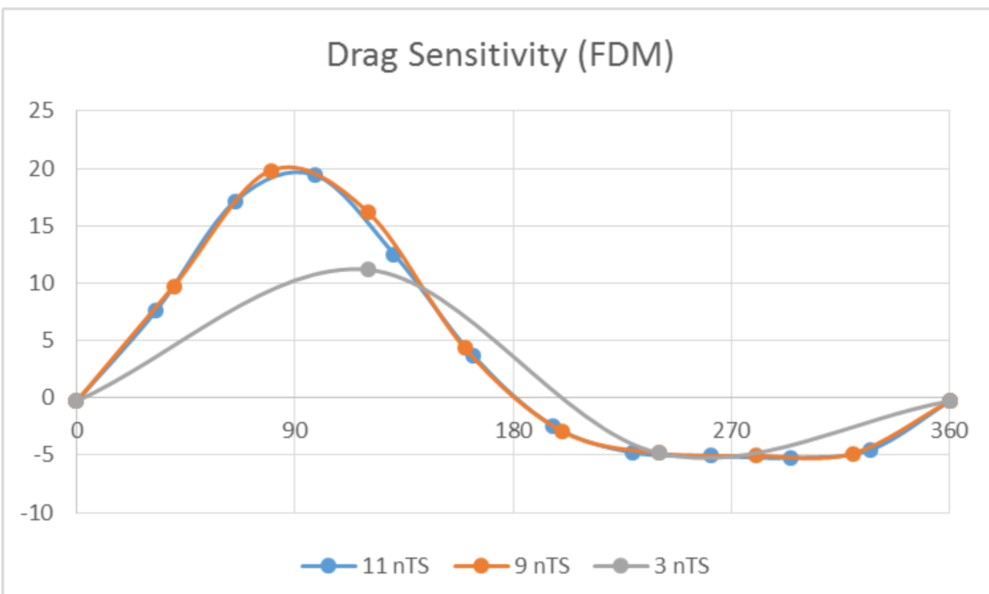

Figure 7.18: Comparison of DRAG sensitivity with 3,9,11 time instances

(11 nTS) shows good agreement. However, they show some discrepancy in lift sensitivities in the advancing side. The blue line (11 nTS) has no data point near 120 degree azimuth angle, so that is the reason why those two lines look different. Figs.7.18 and 7.19 show that

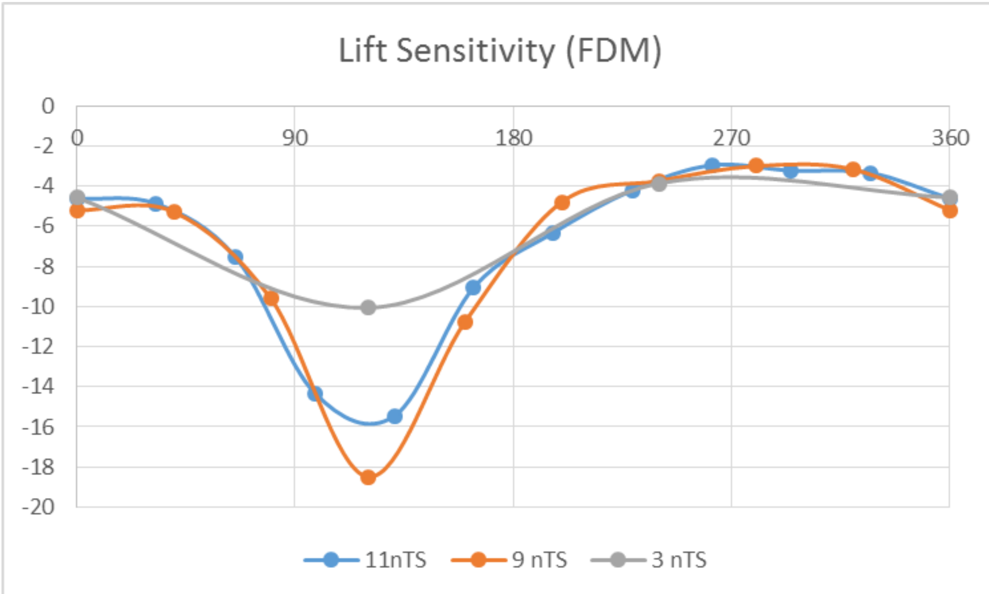

Figure 7.19: Comparison of LIFT sensitivity with 3,9,11 time instances

the time spectral analysis with 9 time instances is good enough to calculate the lift and drag sensitivities.

7.4 Coupled Sensitivity Analysis

The sensitivity analysis in Sections 7.2, 7.3 only account for the air flow changes due to the shape perturbations. With structural state changes (i.e. deformation), generated based on the air flow changes, accurate sensitivity analysis results can be expected. So, the fluid-structure coupled sensitivity analysis is essential for a reliable design framework. Fig. 7.20 shows the fluid-structure coupled adjoint equations. The coupled adjoint Jacobian matrix consists of 2 $\times$ 2 block Jacobians. The first one, $\frac{\partial R}{\partial w}$, is the aerodynamic Jacobian which is used in aerodynamics only sensitivity analysis. It means the partial derivative of fluid residual(R) with respect to the fluid state(w). The size of this sub-matrix is huge (368,640 $\times$ 368,640), but this is a sparse matrix. For the fluid-structure coupled sensitivity analysis, the other three Jacobians should be added. $\frac{\partial S}{\partial y}$ is the structural Jacobian. It means the partial derivative of structural residual(S) with respect to the structural state(y). The size of this sub-matrix is 3,348 $\times$ 3,348. This matrix is a sparse matrix. The third Jacobian is $\frac{\partial S}{\partial w}$. This term is the off-diagonal term and it couples fluid and structure. So, it is called as coupled cross Jacobian. This is the partial derivative of structural residual(S) with respect to the fluid state(w). The size of this sub-matrix is 3,348 $\times$ 368,640. This is a sparse matrix. The last one is $\frac{\partial R}{\partial y}$. This Jacobian is the other off-diagonal term, so it is one of coupled cross Jacobians. This is the partial derivative of fluid residual(R) with respect to the structural state(y). This sub-matrix is the only densely populated matrix. This can be explained by the fact that the structural perturbation (displacement) affects all the volume mesh(x_v) and mesh metrics(s_x) through surface mesh (x_s). Due to the large size of the adjoint matrix,

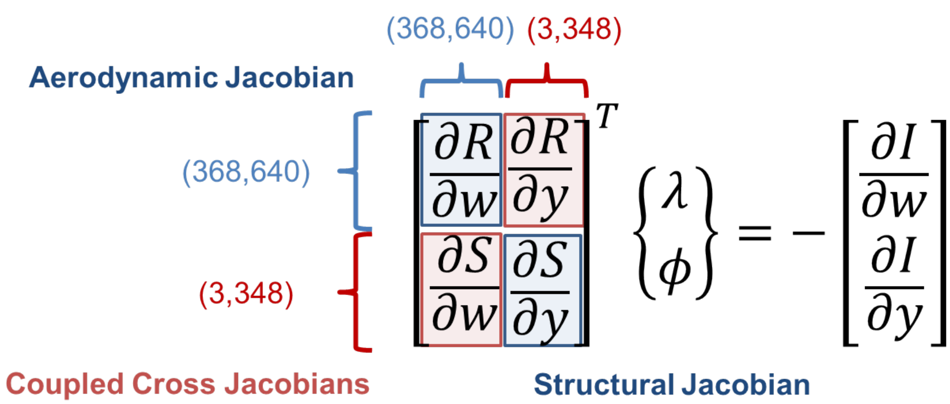

Figure 7.20: Coupled Adjoint Solver

GMRES and Krylov subspace solver has been used to solve coupled adjoint equation. This has been implemented by using PETSC library, which is a suite of scalable and parallel routine for the large scale PDEs. This system takes around 1,500 iterations with 600 restart iterations for the converged solutions. Fig.7.21 shows the comparison between adjoint-based and FMD-based coupled sensitivity analysis results with respect to four different design variables. The objective function of this analysis is the sum of all displacements. For the coupled sensitivity analysis, the sum of displacements is the direct measure of the change of system. So, the displacement sensitivity is used to validate adjoint-based coupled sensitivity analysis. The displacement sensitivities with respect to 69th and 70th design variables are quite well matched with each other. However, the comparison between adjoint and FDM sensitivities shows small discrepancy for 71st and 72nd bumps. This can be explained by the fact that 71st and 72nd bump generated bigger aerodynamic load changes comparing to other bumps in the same airfoil section. For these sensitive design variables, small error source could be magnified then it shows bigger discrepancy than other design variables. Fig.7.22 shows the comparison between adjoint-based and FMD-based coupled sensitivity

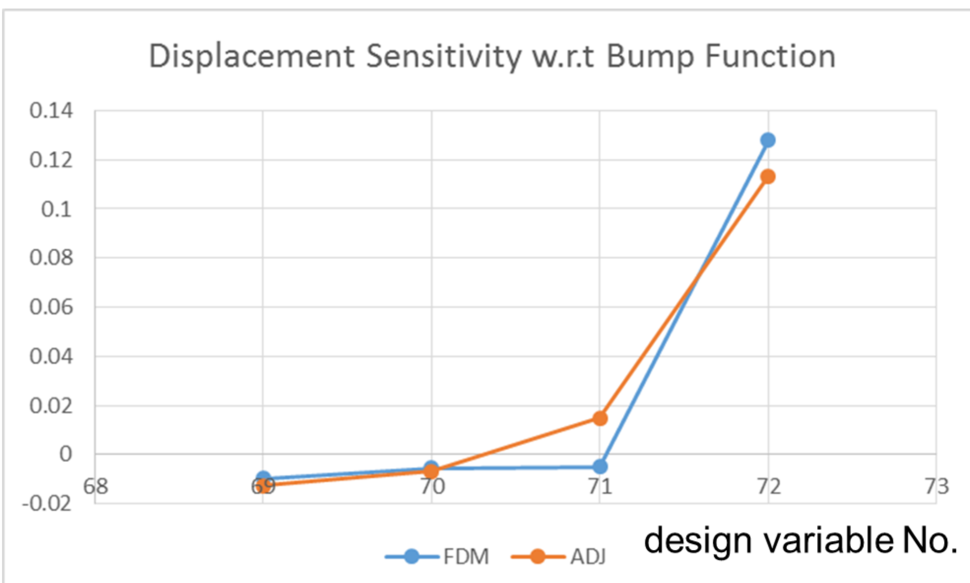

Figure 7.21: Coupled Sensitivity Analysis with respect to four Design Variables

analysis results with 3 time instances. They show good agreement in all 3 time instances. The 69th bump is located on the lower surface of airfoil section.

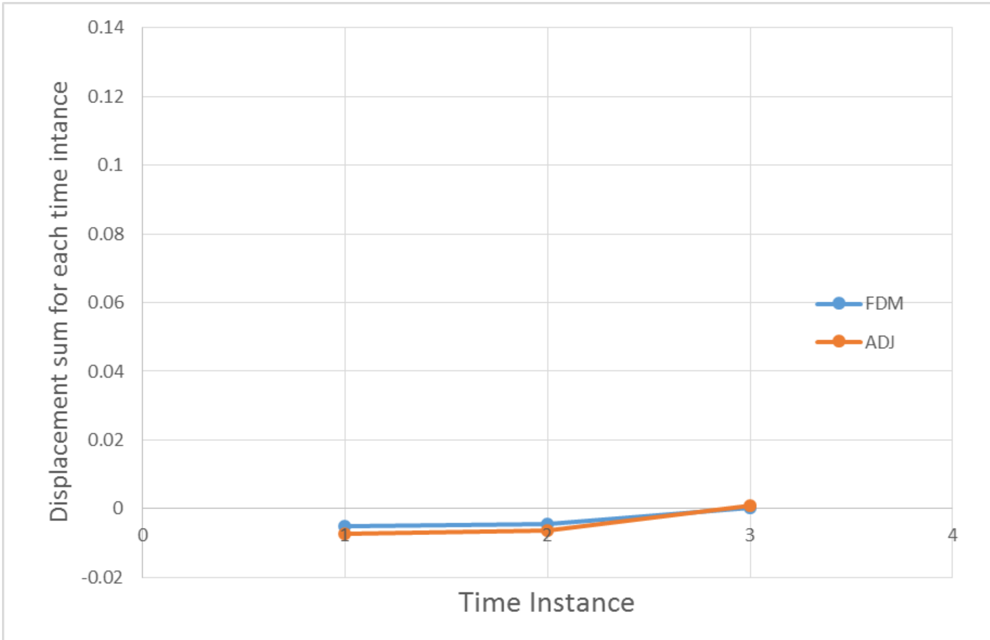

Figure 7.22: Coupled Sensitivity Analysis with 3 time instances

7.5 Future Work

After the development is completed, the fluid-structure coupled adjoint based sensitivity analysis will be used to optimize the shape of the rotor blade. Minimization of required power is pursued as an objective of the optimization problem with constraints on the thrust and drag of the rotor. Therefore, plans for future work involve multidisciplinary design optimization that integrates the CFD/CA coupling procedure. The overall design procedure is shown in Fig. 7.23.

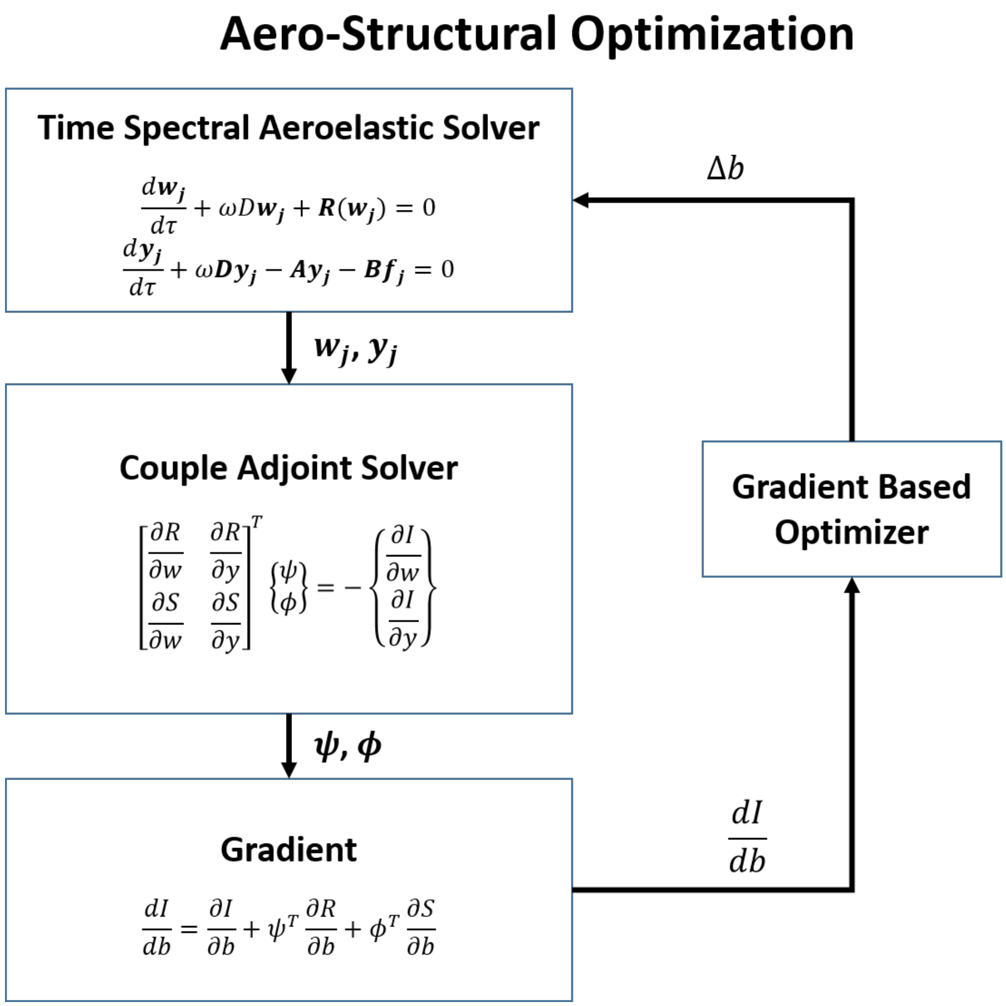

Figure 7.23: Multidisciplinary Design Procedure

Chapter 8

Conclusions

This chapter summarizes the conclusion of this research work. This research focused on the coupled sensitivity analysis combining fluid and structural analysis. The time-spectral approach is used to overcome inefficient calculation of rotor flows by expressing flow and structural state variables as Fourier series with small number of harmonics.

1. Time spectral formulation based fluid-structural governing equations are used for FSI coupled analysis. The governing equations are modified by replacing physical time derivative operator with spectral time derivative operators. There is a difference between fluid and structural time spectral derivative operators due to the fact that nondimensionalized form of structural governing equations are using the azimuth angle as nondimensional time. The derivations of both time spectral derivative operators are shown in Sections 3.3 and 4.2.3 to show the reason why they are different.

2. Coupled adjoint-based sensitivity analysis is discussed in 5.2. This section explains how the adjoint method has become a popular approach for solving design problems with a large number of design variables. The derivations of the adjoint Jacobian matrices are shown including the cross Jacobian terms.

3. The accuracy and the efficiency of flow solver are examined by simulating the flow conditions commonly encountered in a helicopter flight. Time spectral approach is used as an efficient algorithm and applied to the simulation of UH-60A flight condition. A significant

reduction in the computational cost achieved by its Fourier series form of the periodic time response and the assumption of periodic steady state. A good agreement between time accurate and time spectral analysis is noted for the high speed flight condition of UH-60A configuration. Predictions from both methods also agree quite well with the experimental data.

4. Adjoint based aerodynamics only sensitivity analysis results are discussed in 7.2. The gradients of aerodynamics coefficients (Cl and Cd) with respect to the design variables (shape changes due to the bump functions) are computed using adjoint method, also they are compared with the sensitivities from finite difference method. Even with presence of small differences, these two results show a good agreement to each other. Aerodynamics only sensitivity includes the effect of fluid state changes due to the shape changes, but the contributions of structural deformation are not included.

5. FDM based aerodynamics only sensitivity analysis results are shown in 7.3. At first, step size studies are performed to find an optimal size of bump function (design variables) for the finite difference sensitivity analysis. Then, the gradients of aerodynamic coefficients with different number of time instances are compared. The sensitivities with 9 time instances are well matched with the results of 11 time instances, this shows that time spectral analysis with 9 time instances are good enough to simulate the fluid and structural motion of rotor blade.

6. Adjoint based coupled sensitivity analysis results are shown in 7.4. The gradients of structural displacements with respect to the design variables are calculated using adjoint method, and they are compared with the gradients from finite difference method. Even with the presence of small discrepancy for two design variables, they show overall good agreement to each other. Coupled sensitivity analysis includes not only the effect of fluid state changes but also the contribution of structural deformation.

7. The fluid-structure coupled adjoint based sensitivity analysis will be used to optimize the shape of the rotor blade in the future work.

Bibliography

[1] Michael B Giles and Niles A Pierce. An introduction to the adjoint approach to design. *Flow, turbulence and combustion*, 65(3-4):393–415, 2000.

[2] Jacques EV Peter and Richard P Dwight. Numerical sensitivity analysis for aerodynamic optimization: A survey of approaches. *Computers & Fluids*, 39(3):373–391, 2010.

[3] Siva Nadarajah and Antony Jameson. A comparison of the continuous and discrete adjoint approach to automatic aerodynamic optimization. In *38th Aerospace Sciences Meeting and Exhibit*, page 667, 2000.

[4] Thomas D Economon, Juan J Alonso, Tim A Albring, and Nicolas R Gauger. Adjoint formulation investigations of benchmark aerodynamic design cases in su2. In *35th AIAA Applied Aerodynamics Conference*, page 4363, 2017.

[5] Seongim Choi, Kihwan Lee, Mark M Potsdam, and Juan J Alonso. Helicopter rotor design using a time-spectral and adjoint-based method. *Journal of Aircraft*, 51(2):412–423, 2014.

[6] Gunjit Bir, Indeerit Chopra, et al. University of maryland advanced rotor code (umarc) theory manual. *Center for Rotorcraft Education and Research, University of Maryland, College Park, MD*, 1994.

[7] John C Houbolt and George W Brooks. Differential equations of motion for combined flapwise bending, chordwise bending, and torsion of twisted nonuniform rotor blades. 1957.

[8] Robert A Ormiston and Dewey H Hodges. Linear flap-lag dynamics of hingeless helicopter rotor blades in hover. *Journal of the American Helicopter Society*, 17(2):2–14, 1972.

[9] Dewey H Hodges and EH Dowell. Nonlinear equations of motion for the elastic bending and torsion of twisted nonuniform rotor blades. 1974.

[10] Dewey H Hodges, Robert A Ormiston, and David A Peters. On the nonlinear deformation geometry of euler-bernoulli beams. Technical report, NATIONAL AERONUATICS AND SPACE ADMINISTRATION MOFFETT FIELD CA AMES RESEARCH ..., 1980.

[11] Raymond G Kvaternik and Krishna RV Kaza. Nonlinear curvature expressions for combined flapwise bending, chordwise bending, torsion and extension of twisted rotor blades. 1976.

[12] Aviv Rosen and Peretz P Friedmann. Nonlinear equations of equilibrium for elastic helicopter or wind turbine blades undergoing moderate deformation. 1978.

[13] FK Straub and PP Friedmann. A galerkin type finite element method for rotary-wing aeroelasticity. 1980.

[14] Inderjit Chopra and N Sivaneri. Aeroelastic stability of rotor blades using finite element analysis. 1982.

[15] Johnson Aeronautics. Rotorcraft aerodynamics models for a comprehensive analysis.

[16] Hossein Saberi, Maryam Khoshlahjeh, Robert A Ormiston, and Michael J Rutkowski. Overview of rcas and application to advanced rotorcraft problems. In *American Helicopter Society 4th Decennial Specialists' Conference on Aeromechanics, San Francisco, CA*, 2004.

[17] Roger C Strawn and Francis X Caradonna. Conservative full-potential model for unsteady transonic rotor flows. *AIAA journal*, 25(2):193–198, 1987.

[18] Roger C Strawn, Andre Desopper, Judith Miller, and Alan Jones. Correlation of puma airloads: Evaluation of cfd prediction methods. 1989.

[19] Ki-Chung Kim, Andre Desopper, and Inderjit Chopra. Blade response calculations using three-dimensional aerodynamic modeling. *Journal of the American Helicopter Society*, 36(1):68–77, 1991.

[20] Jayanarayanan Sitaraman, JD Baeder, and Inderjit Chopra. Validation of uh-60 rotor blade aerodynamic characteristics using cfd. In *ANNUAL FORUM PROCEEDINGS-AMERICAN HELICOPTER SOCIETY*, volume 59, pages 1452–1468. AMERICAN HELICOPTER SOCIETY, INC, 2003.

[21] Mark Potsdam, Hyeonsoo Yeo, and Wayne Johnson. Rotor airloads prediction using loose aerodynamic/structural coupling. *Journal of Aircraft*, 43(3):732–742, 2006.

[22] ARM Altmikus, S Wagner, Ph Beaumier, and G Servera. A comparison- weak versus strong modular coupling for trimmed aeroelastic rotor simulations. In *AHS International, 58 th Annual Forum Proceedings-*, volume 1, pages 697–710, 2002.

[23] O Bauchau and J Ahmad. Advanced cfd and csd methods for multidisciplinary applications in rotorcraft problems. In *6th Symposium on Multidisciplinary Analysis and Optimization*, page 4151, 1996.

[24] Hubert Pomin and Siegfried Wagner. Navier-stokes analysis of helicopter rotor aerodynamics in hover and forward flight. *Journal of Aircraft*, 39(5):813–821, 2002.

[25] Antony Jameson and John Vassberg. Computational fluid dynamics for aerodynamic

design-its current and future impact. In *39th Aerospace Sciences Meeting and Exhibit*, page 538, 2001.

[26] Antony Jameson. Aerodynamic shape optimization using the adjoint method. *Lectures at the Von Karman Institute, Brussels*, 2003.

[27] Sangho Kim, Juan J Alonso, and Antony Jameson. Multi-element high-lift configuration design optimization using viscous continuous adjoint method. *Journal of Aircraft*, 41(5):1082–1097, 2004.

[28] Dimitri Mavriplis. Solution of the unsteady discrete adjoint for three-dimensional problems on dynamically deforming unstructured meshes. In *46th AIAA Aerospace Sciences Meeting and Exhibit*, page 727, 2008.

[29] Sang Wook Lee and Oh Joon Kwon. Aerodynamic shape optimization of hovering rotor blades in transonic flow using unstructured meshes. *AIAA journal*, 44(8):1816–1825, 2006.

[30] Eric J Nielsen, Boris Diskin, and Nail K Yamaleev. Discrete adjoint-based design optimization of unsteady turbulent flows on dynamic unstructured grids. *AIAA journal*, 48(6):1195–1206, 2010.

[31] Eric J Nielsen, Elizabeth M Lee-Rausch, and William T Jones. Adjoint-based design of rotors in a noninertial reference frame. *Journal of Aircraft*, 47(2):638–646, 2010.

[32] Joaquim R RA Martins, Juan J Alonso, and James J Reuther. High-fidelity aerostructural design optimization of a supersonic business jet. *Journal of Aircraft*, 41(3):523–530, 2004.

[33] Joaquim RRA Martins, Juan J Alonso, and James J Reuther. A coupled-adjoint sensi-

tivity analysis method for high-fidelity aero-structural design. *Optimization and Engineering*, 6(1):33–62, 2005.

[34] Gaetan KW Kenway, Graeme J Kennedy, and Joaquim RRA Martins. Scalable parallel approach for high-fidelity steady-state aeroelastic analysis and adjoint derivative computations. *AIAA journal*, 52(5):935–951, 2014.

[35] Kurt Maute, Melike Nikbay, and Charbel Farhat. Coupled analytical sensitivity analysis and optimization of three-dimensional nonlinear aeroelastic systems. *AIAA journal*, 39(11):2051–2061, 2001.

[36] Kurt Maute, Melike Nikbay, and Charbel Farhat. Sensitivity analysis and design optimization of three-dimensional non-linear aeroelastic systems by the adjoint method. *International Journal for Numerical Methods in Engineering*, 56(6):911–933, 2003.

[37] Asitav Mishra, Dimitri Mavriplis, and Jay Sitaraman. Time-dependent aeroelastic adjoint-based aerodynamic shape optimization of helicopter rotors in forward flight. *AIAA Journal*, pages 3813–3827, 2016.

[38] Asitav Mishra, Karthik Mani, Dimitri Mavriplis, and Jay Sitaraman. Time-dependent adjoint-based aerodynamic shape optimization applied to helicopter rotors. *Rn*, 3:2, 2014.

[39] Arathi Gopinath and Antony Jameson. Time spectral method for periodic unsteady computations over two-and three-dimensional bodies. In *43rd AIAA aerospace sciences meeting and exhibit*, page 1220, 2005.

[40] Edwin Van Der Weide, Arathi Gopinath, and Antony Jameson. Turbomachinery applications with the time spectral method. In *35th AIAA Fluid Dynamics Conference and Exhibit*, page 4905, 2005.

[41] Arathi Gopinath and Antony Jameson. Application of the time spectral method to periodic unsteady vortex shedding. In *44th AIAA Aerospace Sciences Meeting and Exhibit*, page 449, 2006.

[42] Kenneth C Hall, Jeffrey P Thomas, and William S Clark. Computation of unsteady nonlinear flows in cascades using a harmonic balance technique. *AIAA journal*, 40(5):879–886, 2002.

[43] Antony Jameson, J Alonso, and M McMullen. Application of a non-linear frequency domain solver to the euler and navier-stokes equations. In *40th AIAA aerospace sciences meeting & exhibit*, page 120, 2002.

[44] DK Im, SI Choi, E Kim, JH Kwon, and SH Park. Unsteady aerodynamic analysis of helicopter rotor blades using diagonal implicit harmonic balance method. *Journal of computational fluids engineering*, 17(1):70–77, 2012.

[45] Ji-Sung Jang, Seongim Choi, Hyung-Il Kwon, Dong-Kyun Im, Duck-Joo Lee, and Jang-Hyuk Kwon. A preliminary study of open rotor design using a harmonic balance method. In *50th AIAA Aerospace Sciences Meeting including the New Horizons Forum and Aerospace Exposition*, page 1042, 2012.

[46] Seongim Choi, Juan Alonso, Edwin Weide, and Jaina Sitaraman. Validation study of aerodynamic analysis tools for design optimization of helicopter rotors. In *25th AIAA Applied Aerodynamics Conference*, page 3929, 2007.

[47] S Choi and A Datta. Time-spectral method for the cfd prediction of main rotor vibratory loads. In *5th International Conference on CFD*, 2008.

[48] Seongim Choi and Anubhav Datta. Cfd prediction of rotor loads using time-spectral

method and exact fluid-structure interface. In *26th AIAA Applied Aerodynamics Conference*, page 7325, 2008.

[49] Seongim Choi, Mark Potsdam, Kihwan Lee, Gianluca Iaccarino, and Juan Alonso. Helicopter rotor design using a time-spectral and adjoint-based method. In *12th AIAA/ISSMO Multidisciplinary Analysis and Optimization Conference*, page 5810, 2008.

[50] Rachit Prasad, Hyunsoon Kim, and Seongim Choi. Flutter related design optimization using the time spectral and coupled adjoint method. In *2018 AIAA/ASCE/AHS/ASC Structures, Structural Dynamics, and Materials Conference*, page 0101, 2018.

[51] Sicheng He, Eirikur Jonsson, Charles A Mader, and Joaquim Martins. Aerodynamic shape optimization with time spectral flutter adjoint. In *AIAA Scitech 2019 Forum*, page 0697, 2019.

[52] Antony Jameson, Wolfgang Schmidt, and Eli Turkel. Numerical solution of the euler equations by finite volume methods using runge kutta time stepping schemes. In *14th fluid and plasma dynamics conference*, page 1259, 1981.

[53] Kedar Naik. The time-spectral method: A primer. 2011.

[54] Anubhav Datta. *Fundamental Understanding, Prediction and Validation of Rotor Vibratory Loads in Steady-Level Flight*. PhD thesis, 2004.

[55] Ki Hwan Lee. *Design Optimization of Periodic Flows Usuing a Time-Spectral Discrete Adjoint Method*. Stanford University, 2010.

[56] Anubhav Datta and Inderjit Chopra. Validation of structural and aerodynamic modeling using uh-60a airloads program data. *Journal of the American Helicopter Society*, 51(1):43–58, 2006.

[57] William G Bousman. Uh-60 airloads program tutorial. 2009.

[58] R Kufeld, Dwight L Balough, Jeffrey L Cross, and Karen F Studebaker. Flight testing the uh-60a airloads aircraft. In *ANNUAL FORUM PROCEEDINGS-AMERICAN HELICOPTER SOCIETY*, volume 5, pages 557–557. American Helicopter Society, 1994.

[59] WG Bousman, RM Kufeld, D Balough, JL Cross, KF Studebaker, and CD Jennison. Flight testing the uh-60a airloads aircraft. In *50th Annual Forum of the American Helicopter Society, Washington, DC*, 1994.